High resolution, dynamic imaging of early mouse and human liver bud morphogenesis in three dimensions

Tala Mon[1**], Ogechi Ogoke[1**], Daniel Guiggey[1**], Claire Shamul[1], Shatoni Ross[1], Saroja Rao[3], Natesh Parashurama [1,2,6*]

[1] Department of Chemical and Biological Engineering, University at Buffalo (State University of New York), Furnas Hall, Buffalo, NY 14260

[2] Clinical and Translation Research Center (CTRC), University at Buffalo (State University of New York), 875 Ellicott St., Buffalo, NY 14203

[3] Department of Biological Sciences, University at Buffalo (State University of New York), College of Arts and Sciences, 109 Cooke Hall, Buffalo, NY 14260-4610

[6] Department of Biomedical Engineering, University at Buffalo (State University of New York), Furnas Hall, Buffalo, NY 14260

* Corresponding Author

****** These authors contributed equally to this work

Running Title: Imaging 3D liver bud morphogenesis

Contact information:

Natesh Parashurama MD PhD, 907 Furnas Hall, Buffalo, NY 14260; Tel: 716-645-1201; Fax: 716-645-3822; e-mail: nateshp@buffalo.edu

SUMMARY:

BACKGROUND

Liver organogenesis has thus far served as a paradigm for solid organ formation, and human stem cells are being applied to model the process. Murine genetic studies indicate that stepwise morphogenetic changes occur during liver organogenesis. However, analysis of the liver bud is limited typically to 2D tissue sections, which limits visualization and quantitation, and differences between mouse and human liver organogenesis are poorly understood. Therefore, new approaches are needed to elicit further morphogenetic details of liver organogenesis and to compare mouse and human liver bud growth.

RESULTS

To address this need, we focused on high resolution imaging, visualization, and analysis of early liver growth by using available online databases for both mouse (EMAP, Toronto Phenogenomics center) and human (3D Atlas of Human Embryology), noninvasive multimodality imaging studies of the murine embryo, and mouse/human liver weight data. First, we performed three-dimensional (3D reconstructions) of stacked, digital tissue sections that had been initially segmented for the liver epithelium and the septum transversum mesenchyme (STM). 3D reconstruction of both mouse and human data sets enabled visualization and analysis of the dynamics of liver bud morphogenesis, including hepatic cord formation and remodeling, mechanisms of growth, and liver-epithelial STM interactions. These studies demonstrated potentially underappreciated mechanisms of growth, including rapid exponential growth that is matched at the earliest stages by STM growth, and some unique differences between mouse and human. To gain further insight into the observed, exponential liver bud growth, we plotted volumetric data from 3D reconstruction together with fetal liver growth data from multimodality (optical projection tomography, magnetic resonance imaging, micro-CT) and liver weight data to compose complete growth curves during mouse (E8.5-E18) and human (day 25-300). We then performed curve fitting and parameter estimation, using Gompertzian models, which enables the comparison between mouse and human, and liver growth compared to tumor growth.

CONCLUSION

We take a novel approach, 3D reconstruction and high resolution, dynamic imaging of the mouse, and human liver bud during growth. Overall, we demonstrate improved high resolution 3D imaging, under-appreciated and potentially new mechanisms of growth, and complete liver growth curves with quantitative analysis. Our data suggests potential morphogenetic features that enable rapid liver growth and demonstrate structural and quantitative differences between mouse and human liver bud growth. This information can inform approaches to model liver organogenesis using human stem cell-derived organoids.

Keywords: liver development, liver imaging, liver organogenesis, hepatic cords, liver bud, septum transversum mesenchyme, liver tissue engineering, organ development gut development

BACKGROUND

The wide-ranging, global epidemic of chronic end-stage liver disease has garnered increased interest in liver tissue engineering and liver regenerative medicine, including tools for hepatocyte (HEP) culture and expansion, pluripotent and adult stem cell biology, tissue chips to replace liver functions, *in vivo* disease modeling, and drug development (Ogoke, Oluwole et al. 2017). The expansion of liver research into these numerous directions has been sustained by fundamental and seminal studies of hepatic, biliary, and hepatic vascular development, reviewed elsewhere (Zorn 2008). These studies detail key molecular and morphogenetic steps in liver organogenesis, which are intricately linked to the liver bud undergoing rapid liver three-dimensional (3D) growth, leading to rapid growth and eventually, the largest internal organ in the body. If these 3D morphogenetic steps can be further revealed through imaging and quantitative analysis, this can augment approaches in which human stem cell-derived organoids are employed to model liver organogenesis (Koike, Iwasawa et al. 2019).

Seminal genetic studies have established major stages of early liver bud morphogenesis and the dynamic molecular underpinnings that drive these steps. The liver bud is a transient, multicellular structure that arises during E8.5 in mice and ~day 25 in humans, on the scale of 100-200 µm in width and length (Si-Tayeb, Lemaigre et al. 2010). At E8.5, the liver bud contains the liver diverticulum, a ventral out-pocketing of the single cell-layered gut tube, surrounded by a layer of endothelial cells, which itself is surrounded ventrally by the septum transversum mesenchyme (STM) (Si-Tayeb, Lemaigre et al. 2010). At E9.0, the pre-hepatic liver epithelium transitions to a pseudostratified epithelium, and thickens in response to cardiac patterning of foregut endoderm via FGF2 (Ledouarin 1963);(Chen, Tillberg et al. 2015), STM patterning of hepatic endoderm via BMP4 (Rossi, Dunn et al. 2001), and endothelial cells patterning of adjacent foregut endoderm towards hepatic endoderm (Matsumoto, Yoshitomi et al. 2001). Genetic studies demonstrate that transcriptional changes correlate with morphogenetic changes. For example, Foxa2, the first known pioneer transcription factor, is upregulated in hepatic endoderm and primes silent liver genes within hepatic endoderm prior to overt morphogenesis (Lee, Friedman et al. 2005). Hex expression occurs during pseudostratification, prior to hepatic cord formation, which is essential for rapid liver growth (Bort, Signore et al. 2006);(Enzan, Himeno et al. 1997). These hepatic cords form at E9.5 (23-25 somite stage) and are defined as finger-like projections that protrude into the STM, express the master transcription factors Hex (Martinez Barbera, Clements et al. 2000), Prox1 (Sosa-Pineda, Wigle et al. 2000), and Tbx3 (Ludtke, Christoffels et al. 2009), and undergo both EMT (Bort, Signore et al. 2006) and collective cell migration (Cascio and Zaret 1991). These studies

collectively demonstrate that hepatic cords form rapidly and have a short half-life. Despite their importance, existing histological studies demonstrate hepatic cords with a wide range of geometry, location, and thickness (Matsumoto, Yoshitomi et al. 2001, Suzuki, Kanai et al. 2006). To our knowledge, the hepatic cords have not been imaged/visualized in 3D at high spatial resolution in murine or human systems.

The various mesenchymal elements within the liver bud bear a large role in early 3D fetal liver growth and morphogenesis, as borne out by recent scRNA-seq studies (Lotto, Drissler et al. 2020). The STM envelopes the early liver diverticulum in 3D and mediates growth by soluble factor-based induction, leading to transduction of intracellular signals and transcriptional activation. For example, genetic studies of BMP4, Smad2/3 and neurturin (all part of the TGFß superfamily) (Weinstein, Monga et al. 2001), (Tatsumi, Miki et al. 2007), HEP growth factor (HGF) (Schmidt, Bladt et al. 1995), and ephrins (Cayuso, Dzementsei et al. 2016), all demonstrate a role for the inductive properties of STM. Smad 2/3 (TGFß superfamily) haplo-deficient embryos exhibit severely disrupted liver growth by E14.5, due to both loss of ß1-integrin (a known TGFß, target) expression, and mislocalized E-cadherin expression (Weinstein, Monga et al. 2001). HGF knockout studies are mediated by a lack of c-met receptor engagement in hepatoblasts (Schmidt, Bladt et al. 1995). Further, GATA4 -/- embryos lack STM, hepatic cord formation, and subsequent liver development (Watt, Zhao et al. 2007). Knockout of Hlx1, which is strongly expressed within the STM, does not affect early liver specification and hepatic cord formation, but greatly affects 3D liver expansion (Lints, Hartley et al. 1996). Finally, ARF6 knockout disrupts cell membrane polarization, and receptor recycling in liver epithelia (Suzuki, Kanai et al. 2006). In addition to the STM, hematopoietic stem cells, which seed the fetal liver at ~E11.0, and at 5-6 weeks in human liver, play a role in liver growth. The absence of fetal liver hematopoiesis leads to complex liver morphological effects with mixed phenotypes (Yagi, Deguchi et al. 1998), while affecting liver maturation via the cytokine Oncostatin M (OSM) (Yoshimura, Ichihara et al. 1996), (Kamiya, Kinoshita et al. 1999). Finally, endothelial cells within the developing sinusoids also play a key role in inductive liver growth (Collardeau-Frachon and Scoazec 2008). The absence of endothelial cells in flk -/- mice inhibits liver growth, and *in vivo* studies of explanted mouse liver bud demonstrate that endothelial-lined, branched microvasculature induces 3D liver bud outgrowth even in the absence of blood flow (Matsumoto, Yoshitomi et al. 2001). Moreover, VEGF-A, HGF, IL-6, and Wnt are collectively secreted from sinusoidal endothelial cells and signal to HEPs *in vivo* (LeCouter, Moritz et al. 2003). Taken together, these studies convey the strong inductive, role mesenchyme in 3D fetal liver growth and organogenesis, although imaging/visualization mesehnchyme during early liver bud growth has not been achieved (Gordillo, Evans et al. 2015);(Tanimizu and Mitaka 2017);(Zorn 2008);(Ober and Lemaigre 2018).

Despite the significance of 3D liver morphogenesis, there have been a lack of studies that determine morphogenetic features in 3D. Established techniques include immunohistochemistry, but this only enables 2D rather than 3D visualization of structure, is highly dependent upon tissue preparation and sectioning angle, and exhibits inter-subject variability (Matsumoto, Yoshitomi et al. 2001, Suzuki, Kanai et al. 2006). To assess human fetal liver growth, scientists have used liver weights or liver morphometry (Szpinda, Paruszewska-Achtel et al. 2015) which don't enable visualization at the earliest stages, or noninvasive imaging approaches, like ultrasound (Pardi and Cetin 2006, Chen, Tillberg et al. 2015), which lack spatial resolution to image morphogenesis. Noninvasive imaging of liver bud morphogenesis is challenging to perform *in utero* due to tissues, fluids, subject motion, and breathing artifacts. Nonetheless, noninvasive embryo imaging approaches (Nieman, Wong et al. 2011) like light sheet microscopy, (Udan, Piazza et al. 2014), ultrasound (Phoon 2006), optical coherence tomography (OCT) (Syed, Larin et al. 2011), micro-computed tomography (CT) (Wong, van Eede et al. 2015), magnetic resonance imaging (MRI) (Turnbull and Mori 2007), photoacoustic tomography (Turnbull and Mori 2007), optical projection tomography (Lickert, Takeuchi et al. 2004) have been employed. Overall, dynamic imaging has been challenging, and there is still a need for high spatial resolution (~1-10 µm), dynamic (high temporal resolution), and small field of view imaging to image dynamic events in morphogenesis.

The E-mouse atlas project (EMAP) started with a concerted effort for 3D digital visualization of anatomy, histology, and gene expression during embryogenesis (Baldock, Bard et al. 1992), and the 3D Atlas of Human Embryology project followed (de Bakker, de Jong et al. 2016). We hypothesize that these digital resources, as well as others (Toronto Phenogenomics center), and mouse and human liver volume data could be used to better image and visualize early liver morphogenesis and/or estimate liver volumes. Analysis of the liver bud is limited typically to 2D tissue sections, which limits visualization and quantitation, and differences between mouse and human liver organogenesis are poorly understood. Therefore, new approaches are needed to elicit further morphogenetic details of liver organogenesis and to compare mouse and human liver bud growth. We focused on high resolution imaging, visualization, and analysis of early liver growth by using available online databases for both mouse (EMAP, Toronto Phenogenomics center) and human (3D Atlas of Human Embryology), noninvasive multimodality imaging studies of the murine embryo, and mouse/human liver weight data. We demonstrate improved high resolution 3D imaging, under-appreciated and potentially new mechanisms of growth, and complete liver growth curves with quantitative analysis.We believe that this will improve our understanding of liver organogenesis. This 3D visualization enables further investigation into the multicellular and mesenchyme specific signals necessary for normal liver organogenesis and microarchitecture (Watt, Zhao et al. 2007);(Zhao, Watt et al. 2005);(Margagliotti, Clotman et al. 2007).

METHODS

Mouse liver development data visualization, three-dimensional reconstruction, and analysis

Aligned and registered image slices from each desired time point were downloaded from eMouseAtlas database and e-Mouse Atlas Project (EMAP, emouseatlas.org), (Baldock, Bard et al. 1992) in WLZ format (Richardson, Venkataraman et al. 2014). An outline of the process of data acquisition and analysis is shown (**Figure 1**). In this database, embryos were prepared by fixation, clearing, and embedded in wax, sectioned, stained and mounted on slides. Specimens ranged from 244 to 869 slices with 4 µm per pixel in the x and y dimensions, and 7 µm in the z dimension. The WLZ files were developed from H&E stains of mouse embryos. Each time point was based on one specimen, for a total of (n = 11) mice. Slices were converted to NII format which preserves the scaling of micrometers to pixels for import into ImageJ (https://imagej.nih.gov/). We first located the gut tube within each mouse as a hollow void, extending throughout the specimen. The liver bud starts as the liver diverticulum which is the ventral outpocketing of the gut tube found by locating the liver diverticulum (denoted in the software) surrounded by mesenchyme. We confirmed this is the liver bud by distinguishing it from the lung bud (superior) and ventral and or dorsal pancreatic buds (inferior). A distinct border can be seen of thickened tissue that was identified to be the walls of the liver diverticulum and it and everything inside leading up next to the gut tube was segmented as the liver. The STM is considered to be the surrounding tissue around the thickened epithelial evident from the H&E slides.

We referenced published immunofluorescence of liver (stained for Hnf4a, and Hex) bud tissue to determine relative tissues boundaries of mesenchyme and developing liver bud (Margagliotti, Clotman et al. 2008);(Bort, Signore et al. 2006), existing textbooks and online resources of mouse and human developmental biology to color-code our data sets and reflect accurately *in vivo* representation, (**Figure 1-2, Supplemental Figures 1-3)** Therefore, using Segmentation Editor, pre-tagged developing liver, septum transverse mesenchyme (STM), and the gut tube, were segmented arbitrarily into green, red, and yellow, respectively. E8.5 contained only pre-segmented areas of the liver diverticulum and gut tube, but not the STM. Each 3D object was generated from different EmouseAtlas specimens (EMA). For the E8.5 mouse Theiler Stage (TS) 13, EMA13 was used, at E9.0 (TS14), EMA14 was used, at E9.5 (TS15), EMA28 was used, and at E10.0 (TS16), EMA38 was used. In these specimens, 3D reconstruction of the existing liver bud was performed using the 3D data set which enables the selection of gut tube endoderm, hepatic endoderm, and STM. 3D imaging of the 3D reconstructed mouse liver bud within the whole embryo was unfortunately unable to illustrate significant images of liver bud morphogenesis (**Figure 1-2,**

Supplemental Figure 1-3). To focus the field of view to the liver bud only, the embryo was removed from view. When the STM or gut tube was obscuring the liver bud, the opacity of these tissues was reduced to 50%. Light and shading were at default settings and movies were recorded using the built-in tool of ImageJ 3D Viewer. Movies were created by 2 frames per degree of rotation and exported at 7 fps at a resolution of 512 x 512 pixels.

For calculations of mouse liver volume, we also downloaded MRI volumetric data from the eMouseAtlas database and e-Mouse Atlas Project (EMAP, emouseatlas.org) (Baldock, Bard et al. 1992) in WLZ format (Richardson, Venkataraman et al. 2014). This MRI volume data included E9.5 (n = 2), E10 (n = 1), E10.5 (n = 2), E11.0 (n = 1), E11.5 (n = 1), E14.0 (n = 1), E18.0 (n = 1). In addition to the mouse embryo image stacks obtained from the e-Mouse atlas, we also acquired volumetric data from the Toronto Centre for Phenogenomics's Mouse Imaging Centre for E11.5, E12, E13, and E14 (http://www.mouseimaging.ca/). This data was obtained using optical projection tomography (OPT) and computed tomography (CT). For OPT data, volume data was obtained for E11.5 (n = 1), E12 (n = 1), E13 (n = 1), and E14 (n = 1). For CT data, volume data was obtained for E15.5 (n = 35). The mouse number obtained from each analysis approach (**Table I**) and the voxel dimensions (**Table II**) are shown. The mouse strains were C57/BL6. Using the same procedure, we performed 3D reconstruction followed by calculation of the volume as above.

3D reconstruction and visualization of human liver bud

For the human development, grey image slices of the aligned and registered H&E stains were downloaded from the 3D Atlas of Human Embryology (3dembryoatlas.com) along with the label files (de Bakker, de Jong et al. 2012). 3D Atlas of Human Embryology utilizes about 15,000 sections, which were digitized and aligned with the software package Amira to create image stacks. Grey and label files are imported into ImageJ using the TrakEM2 plugin and the scaling of micrometers to pixels is set using values provided by the authors. The STM was segmented manually, and visualized from histological sections, whereas for the developing liver and the gut tube we used the pre-existing segmentation. All segmented regions are exported as image stacks in TIFF format. 3D reconstruction was performed by importing the stacks into the 3D Viewer plugin with a smoothness factor of 10. Pixel values for each time point (Carnegie stage) are listed (**Table III**). Movies were created by 2 frames per degree of rotation and exported at 7 fps at a resolution of 512 x 512 pixels.

Calculation of mouse and human volumes from liver weights

We also obtained mouse and human liver weight data and estimated volumes from weights. Mouse liver weight data was acquired for E13, E14, E15, and E18 (Nomura 1976). Additional mouse liver weight data

was acquired from (Kamei, Tsutsumi et al. 1999) and (Song, Luo et al. 2008)for E13 and E14.5 respectively.

Human fetal volumes (n=69) were obtained (Szpinda, Paruszewska-Achtel et al. 2015) in addition to liver weight data (n=861) (Man, Hutchinson et al. 2016). The human liver weight data were obtained from human fetuses from (Man, Hutchinson et al. 2016) for days 84 through 294. To account for the growth-restricted liver weights in (Man, Hutchinson et al. 2016)**,** the bottom 10th percentile of the data was removed. The bottom 10th percentile was determined by finding the 4th order polynomial regression line for the liver weight data to find points furthest from this curve. Since the noise increases proportionally with the volume, the error for each data point was adjusted by the factor $1/V$. The 96 points out of the 957 data points with the highest negative error were removed from further analysis. By assuming the liver has a density of water (1 gm/cm^3), the liver volume was able to be estimated for each liver weight.

Calculation of volumes and surface area of embryonic structures

Using the 3D Manager plugin within ImageJ, volume and surface area were measured with the Measure 3D option after loading the image stacks.

Estimation of cellular density in the gut tube, liver, and STM

For each region, the original histology was examined and imported into ImageJ. Random sections of each region were selected, and the number of cells was counted. This count was divided by the area of the sections. It was assumed that the height of each cell was 10µm and further divided by a height estimation of 10 µm, to give a value of cells per cubic micron, a single cell volume of 1000 um^3, as done previously (Semeraro, Cardinale et al. 2013). We also estimate cell density of the liver based on the adult liver (Ogoke, Oluwole et al. 2017). These are listed (**Table IV**).

Statistical method, linear regreassion analysis and Gompertz modelling

Linear, exponential, logistic, and Gompertz regression models were tested as models for our liver development growth data. The Gompertz model was found to produce the highest coefficient of determination (r^2) and lowest root mean square error (RMSE) for our data and thus was chosen as the model to fit the data. Gompertz has been used as a model for liver tumor growth (Yang, Gao et al. 2020), (Mehrara, Forssell-Aronsson et al. 2013). The Gompertz model can be described as $V = V_o e^{\frac{b}{a}*(1-e^{-at})}$ where V_o is the initial volume, b and a are constants, and V is volume with respect to time t. In this analysis, volume estimates for mouse and human livers were plotted against dpc and examined by non-linear regression analysis against Gompertz growth curve. GraphPad Prism software (GraphPad Software Inc., San Diego, CA) was used to estimate the constants to fit the data as well as find r^2-values, RMSE, p-

values, and confidence intervals. The parameters were estimated by least squares regression. The sum-of-squares of the distances from the curve was also weighted by 1/*V*, since the magnitude of error was found to increase proportionally with the magnitude of the volume. This analysis was done for both mouse and human liver growth. The mouse analysis was done with all the multimodality volume estimates (n=59) as well as with the estimated volumes from liver weight data Nomura et al. (n=10) (Nomura 1976), Kamei et al. (n=20) (Kamei, Tsutsumi et al. 1999), and Song et al. (n=11) (Song, Luo et al. 2008). The human embryo 3D reconstruction volume estimates (n=9) were analyzed together with measured human fetal volumes (n=69) (Szpinda, Paruszewska-Achtel et al. 2015) as well as liver weight data (n=861) (Man, Hutchinson et al. 2016).

RESULTS

3D dynamic imaging of early liver bud morphogenesis.

To image the murine liver bud at high resolution in 3D, we performed 3D reconstructions of stacked, digital, cleared, hematoxylin and eosin (H& E) tissue sections from mouse development at key time points (E8.5, E9, E9.5, and E10) and analyzed the 3D images. At each time point, we segmented each tissue section, targeting the liver epithelium, gut tube, and STM. Upon analysis, the liver bud epithelium is distinct and clearly visualized (green), and demonstrates the gut tube (yellow), the STM (red), and the liver bud (green) (**Figure 1A, E9.5**). Using these representative, segmented sections, together with segmented images for E8.5, E9.0, E9.5, and E10 (**Supplementary Figs 1-3**), we first 3D reconstructed the entire embryo in 3D, which enabled visualization of the colored liver bud and gut tube (**Figure 2A).** These images clearly demonstrate growth in the embryo and liver bud, but liver epithelial morphogenesis (green) could not be visualized, whereas the STM (red) and gut tube (yellow) are clearly visualized (**Figure 2A**). To visualize the liver bud dynamics over time, we reduced the field of view to reveal only the 3D liver bud epithelium, STM, and gut tube (**Compare with Figure 2B with 2A**). When viewed as part of the gut tube, the E8.5 liver epithelium appears as a triangular sheet of cells (**Figure 2B, E8.5**) with tube-like and flat sheet-like regions, which we estimate to be approximately 295 µm (base) x 288 µm (height) x 75 µm (thickness). Although there is known to be transitional epithelium with varying cell size in the liver epithelium (Sherwood, Chen et al. 2009) (**Supplemental Figure 4, Supplemental Video 1-2**), we estimate approximately 3186 cells in the E8.5 liver bud, assuming a single cell volume of 1000 um^3, as done previously (Semeraro, Cardinale et al. 2013). Our morphogenesis analysis of 3D liver bud demonstrates an elliptical shape at E9.0 in the cranial/caudal direction, with a rapid transition to an elliptical shape in the lateral direction at E9.5-E10.0 (**Figure 2B, Compare E9.0, E9.5, and E10**).

Imaging of migrating hepatic cords and sheet-like growth in the developing mouse liver bud.

Having imaged liver bud remodeling in 3D, our goal was to visualize more miniature aspects like the hepatic cords and morphogenetic features. We removed the gut tube from images by segmentation and focused only on the liver bud. With 3D reconstruction and multiple rotated views of the E9.0 liver bud, we observed numerous miniature finger-like projections with dimensions of 1-10µm in length/ diameter (**Figure 3A-B (arrows), Supplementary Video 2**). We also observed sheet-like growth, arranged in a series of ridges spaced between 20-30 µm, at E9.0, from the superior to the inferior portion of the liver bud (**Figure 3C**, **Supplementary Video 2**). Since the original specimens range from 244 to 869 aligned (image registered) slices and the z dimension (height) interslice distance 7 µm in the z dimension, these sheet-like ridges are not a result of imaging artifact or artifacts associated with stacking. They are not a result of interpolation since interpolation was not performed, and they are not due to loss of liver bud tissue during sectioning, since images are based on whole embryo tissue slices. Importantly, the sheet-like ridges do not appear in the images of the gut tube. At E9.5, we observed slightly larger finger-like projections (5-10 µm) (**Figure 3D-E, Supplementary Video 3**), indicating 3D growth, and sheet-like 3D growth arranged in larger ridges at E9.5 compared to E9.0 (**Figure 3E, Supplementary Video 3**). Our data at E10 represents liver bud tissue in which liver epithelial cells (hepatoblasts) and mesenchymal cells intermingle. The E10 liver bud demonstrates numerous interconnections cells that form a sponge-like, trabeculated tissue (**Figure 3F-H, Supplementary Video 3**). These sponge-like inter-connections are observed in, lateral and caudal-cranial directions (**Figures 3F-H, Supplementary Videos 4 and 5**), but not in images of the gut tube. Overall, we demonstrate 3D hepatic cords and a sheet-like growth pattern at E9.0-9.5, and further hepatic cord formation and trabeculation by E10.

Quantification of 3D liver bud volumetric growth

The liver bud leads to rapid expansion to result in the largest organ in the body, but it has not been formally determined how rapid embryonic liver bud growth (E8.5-11.5) matches with fetal liver growth (E12-18). To determine this connection, we employed data not only from 3D reconstructed tissue sections, but also from micro CT, OP imaging, MRI, and data from published liver weights to validate our approach. To add additional data at multiple time points, we identified studies that had measured normal fetal liver weights (Nomura 1976),(Kamei, Tsutsumi et al. 1999),(Song, Luo et al. 2008). To convert weight data to volume data, we assumed a density equal to water (1 g/mL). We performed a growth analysis of the liver by analyzing liver volume growth over time. The data demonstrated a clear, exponential increase in growth over 5 orders of magnitude (**Figure 4A**, **Table V**). This data agrees with our estimation of growth using E8.5 to E18 measurements from 2D images (data not shown). To better visualize these growth changes, we normalized the data (**Figure 4B)** and performed a nonlinear

regression analysis on both the absolute (R^2 = 0.85, and P < 0.001, RMSE = 11,418,126,684) and normalized data absolute (R^2 = 0.85, and P < 0.001, RMSE = 32911,) with a Gompertz model (**Figures 4C-D**). Our analysis demonstrated a correlation coefficient of 0.92 (**Figure 4C**). We wanted to estimate cell count to place our results in context. We estimated cell number using both an estimated cell size of (10^3 μm^3) (Semeraro, Cardinale et al. 2013), as well as cell density of adult livers (Ogoke, Oluwole et al. 2017) and calculated cell counts based on volumes (**Table V**). These two approaches demonstrated estimated cell numbers that differed but were of the same order of magnitude. Fetal livers between E11 and E18 show more uniform growth, unlike the embryonic liver, based on views after 3D reconstruction (**Figure 4E**).

3D imaging of STM-epithelial interactions and growth during murine liver bud development

There is a renewed interest in mesenchyme interactions during liver organogenesis (Lotto, Drissler et al. 2020). Since the STM plays a large role in liver growth, we visualized interactions, with a variety of views, between STM and liver at E8.5 (**Figure 5A-C, Supplemental Video 6)**, E9.0 (**Figure 5D-F, Supplemental Video 7),** E9.5 (**Figures 5G-I, Supplemental Videos 8**), and E 10.0 (**Figures 5J-K, Supplemental Video 9**). Throughout E8.5-10, we found that in all cases STM envelops the liver bud, particularly at E9-10. We also observed that STM is not present on the dorsal part of the liver bud (**Figures 5I and 5L**). Finally, the STM appears to increase in size between E8.5-E10. We quantified the relative and absolute growth of the STM. We observed an 8.8 x 10^2-fold increase in STM volume, as compared to 8.06 x 10^2-fold increase in liver bud volume, over the same time period (**Figure 5A-B**). Overall, the data demonstrated that the STM mirrors the growth pattern of the mouse liver bud between E8.5-E10, and continues to envelop the liver bud with time.

3D imaging of migrating cords and sheet-like growth in the developing human liver bud

To our knowledge, there are few if any studies of human liver bud growth, which may differ from mouse. Imaging of the human 3D reconstructed liver demonstrates extensive lateral growth on days 28 and 33 (**Supplementary Figure 7A-C**), and by day 33, we found that the liver epithelium (green) was indistinguishable from the STM (**Supplementary Figure 7C**). The day 25 liver bud demonstrates numerous 3D cellular projections consistent with hepatic cords in multiple directions (**Figures 6A-C, Supplemental Videos 10-11**). Interestingly, we again notice here not only narrow hepatic cords but also prominent sheet-like structures at multiple levels, particularly visible in anterior-lateral-inferior and anterior-lateral-superior views (**Figures 6A-C**). These cords and sheet-like structures were not due to artifacts of 3D reconstruction. For example, they are not present in the gut tube images of the same reconstructed images, and data was once again stacked, but not interpolated between tissue sections.

More details are regarding this concern are presented in the "Discussion" section. These cords and sheets continue to be present at Day 28 (**Figures 6D-F, Supplemental Videos 12-13**) in multiple views, with a large sheet present in the ventral direction (**Figure 6E**) with clear layering or stacking of sheet-like projections (**Figure 6F**). By Day 33, the liver surface has smoothened and greatly enlarged (**Figures 6G-H, Supplementary Figures 7-8, Supplemental Videos 14-15**). At this time, the liver demonstrates a 3D ellipsoid shape with a lateral axis of ~3500 µm and ~1000 µm in the cranial/caudal direction, indicating extensive lateral growth. We imaged inside the 3D reconstructed liver to analyze interconnections, and observed portions of the liver in enclosed spaces, which appear as green as enclosed spaces (**Figure 6I, Supplementary Videos 16**). We quantified liver growth between day 25 and day 294 using the volume estimations from these 3D reconstructions, as well as published liver volume data (Szpinda, Paruszewska-Achtel et al. 2015) and liver weight data (Man, Hutchinson et al. 2016). We performed a non-linear regression analysis with this data to fit a Gompertz curve ($R^2 = 0.84$, $P < 0.001$, RMSE = 3,087,758) (**Figure 6J**) and for normalized to day 25 (**Figure 6K**) ($R^2 = 0.84$, $P < 0.001$, RMSE = 1037). The data demonstrates a 2.41×10^3–fold change in volume between day 25 and day 50, which is less than the 1.1×10^4–fold change we measure from E9-E14 during mouse development (**Compare Figure 6K with Figure 4D**).

3D imaging of STM-epithelial interactions during human liver bud development

We reconstructed the liver bud together with STM to image their interactions. We analyzed several views on Day 25 (**Figures 7A-E, Supplemental Videos 17-18**) and Day 28 (**Figure 7F-H, Supplemental Videos 19-20)**. The human liver bud at Day 25 demonstrates that STM envelops the liver bud and extends all major directions (**Figures 7A-E, Supplemental Videos 17-18**). The human liver bud at Day 28 demonstrates that STM has grown compared to day 25, but also is several aspects of the STM have been (**Figures 7F-H).** We quantified the STM growth compared to the liver growth on Day 25 and Day 28. The STM size increased by 0.54-fold, while the liver increased by 6.8-fold **(Figure 7I**).

DISCUSSION

Scientists are particularly interested in modeling liver organogenesis *in vivo* for basic science, disease modeling, drug development and discovery, and therapeutic purposes, but many questions remain regarding liver organogenesis and interspecies comparisons. We do not fully comprehend how massive growth of the embryonic and fetal liver occurs and the underlying morphogenetic mechanisms involved (Koike, Iwasawa et al. 2019), nor have we fully elucidated the role of mesenchyme in this process (Lotto, Drissler et al. 2020). To answer these questions, we focused on high resolution, 3D dynamic imaging of

hepatic cord formation, mesenchymal-liver epithelial interactions, and fetal liver growth in both mouse and humans. To image 3D liver bud morphogenesis at a high spatial resolution, we performed 3D reconstructions of dynamic 2D imaging data. This enabled imaging of both murine and human hepatic cords in 3D, for the first time, and comparison of structural differences. We identified morphogenetic features associated with growth, including 3D hepatic cord formation, sheet-like growth, and lateral growth. We further connected liver volume data between embryonic liver and fetal liver in mouse and human systems and performed quantitative modeling and analysis of liver growth. This growth analysis elucidates that growth occurs rapidly and exponentially over several orders of magnitude. We also demonstrate that the STM increases in size during early fetal liver growth, which is highly interconnected with liver epithelium, and that it can have strong local effects on growth and remodeling. Overall, we provide several findings that contribute to our understanding of liver organogenesis.

Embryonic and fetal liver growth establishes the early tissue architecture of the hepatic, biliary, and vascular components of the liver. Our data suggests that the mouse liver undergoes an overall 8.74 x 10^4-fold-increase in volume **(Figure 3B**) between E8.5 to E18. Further, we found a 7.5 x 10^3 change in volume from E9-E14, which corresponds to a 2.5 x 10^4–fold change in volume between day 25 and day 56 in humans. This is in contrast to our data at later stages of liver growth which demonstrates an approximate 7.3-fold increase in volume (**Figure 6K**) (Szpinda, Paruszewska-Achtel et al. 2015) between day 126 and 210 (18 weeks to 30 weeks). These data are consistent with studies with proliferative capacity that demonstrate embryonic day 14 (E14) fetal rat HEPs (rat F-HEps) are still proliferating after 6 months (or the equivalent of 12 human years) with full rat liver repopulation (Dabeva, Petkov et al. 2000). However, studies of E18 rat F-Heps or phenotypically isolated rat E19 fetal hepatic progenitors were shown more recently to repopulate ~1/3 the liver mass in acute models (Boylan, Francois-Vaughan et al. 2017) and chronic models (Bin, Ma et al. 2012). This suggests potentially complex mechanisms involving suppression of proliferation, cell death, and organ size control that regulate growth at fetal stages.

A key finding is that we report high resolution imaging of the 3D hepatic cords in humans and mice. Interestingly, we observe hepatic cords at an earlier stage in mice (E9.0) than previously reported (E9.5). This is possible because our technique has a higher spatial resolution than tissue sectioning, and samples the entire volume of the liver, rather than a single section. Our 3D data agrees with existing data and confirms that these cords migrate to form the trabeculated liver by E10.0 (**Figure 3H**). It remains to be determined how the 3D hepatic cords form the trabeculated liver, as this occurs very rapidly between E9.5 and E10. Thus improved high temporal and spatial resolution imaging is required between these time points to further elucidate these mechanisms. Our data suggests that the human liver bud generally has more hepatic cords than the mouse, and more predominantly in the lateral directions. This could be

because the liver grows even larger in humans, and lateral growth is a key mechanism. Further, we observed these hepatic cords merging into sheets in the human liver, prior to trabeculation, in both mouse and humans. We speculate that this additional “sheet morphogenesis” step may be critical for exponential growth which occurs in the mouse and human liver. Previous studies have used the term “sheet-like” growth in early fetal liver cultures (Hussain, Sneddon et al. 2004), and the term HEP sheets have been used to describe mature liver architecture. While hepatic cords have been described to form hepatic sheets that flank the sinusoids, it is unclear if “sheet-like morphogenesis” has been identified or imaged. From our images, it is also unclear if there are layers of mesenchyme between the observed sheets, which would be an interesting subject of a future study.

Our analysis demonstrates the importance of interactions between the emerging liver epithelium and the STM. Interestingly, our data indicates the murine STM grows at a nearly identical rate to the liver bud between E8.5-E10, and the absolute volume of the STM slightly larger than that of the liver bud from E8-E10. These two facts are not obvious from the approach of traditional tissue sections. While STM expresses inductive signals like BMP, the expanding STM indicates the complex role of the STM and potentially reciprocal signaling between the hepatic endoderm/hepatoblasts. This is consistent with the role of GATA6 and GATA4 within the STM, in which GATA6 and GATA4 knockout via tetraploid blastocyst complementation demonstrates loss of STM mass and inhibits early liver bud development (Watt, Zhao et al. 2007);(Zhao, Watt et al. 2005). Our analysis indicates that large portions of the STM are in a remote location from the liver bud, raising questions of what their role is, because of potential diffusion limitations. Further, human liver bud formation suggests that after sheet-like growth, the STM has been obliterated and internalized laterally, while not in the anterior directions. This strongly suggests the STM may play a role in sheet formation and incorporation of the STM into the liver (**Figure 7H**). However, we can only speculate regarding the mechanisms by which the STM may accomplish this. Another potential role of the STM is in contributing to liver bud remodeling, and not just growth. Ultimately, our objective was to provide a critical analysis of liver bud development in murine and human models. We provided a detailed visualization of these interactions for readers to continuously ponder or investigate unknown liver bud phenomena. In one aspect, it’s quite possible that STM interactions are not equally important in human and mouse development. In one of our new findings, we observed and quantified that the STM grows with the liver, not previously stated in liver bud literature. Therefore, we believe there is a pivotal role for imaging in understanding STM-liver bud interactions.

It is important to note that the finger-like projections and/or sheet-like structures we observe in both liver bud imaging and mesenchyme imaging studies could be confounded with artifacts of tissue sectioning or of 3D reconstruction. Here we discuss several problems pertaining to this issue and try to provide evidence that these factors are not responsible for generating the images that we have obtained.

First, both mouse and human data sections were whole embryo sections (not at the organ level) and reconstructed with appropriate voxel size without the use of interpolation. In other words, the 3D slices were stacked on top of each other and at the correct sizes, but no data was created or interpolated between slices. Any smoothing functions in the software were not at the level of pixel size (µm) and therefore did not remove the sheet-like structures and protrusions that we observe. Error due to rotation of the slices is minimal, because the object was fixed and sectioned, and images were co-registered in the dataset itself. During sectioning of the tissue, there could be some physical displacement of the tissue, that when reconstructed would no longer remain, and this may be responsible for some of the layering effects that can be seen (**Figure 3C and Figure 6B/D)**. We would expect these errors to be on the scale of the sectioning blade itself. However, the sheet-like structures we observe in the human liver bud, are on the order, of 10-20 µm, while thin sectioning blades are on the order of 250 µm. A simple wrinkling effect can be observed in the mouse and human gut tube (**Figure 2B and Figure 6)** but sheet-like growth and formal protrusions are not observed in the area of the liver bud, indicating that these processes are likely unique to the liver. It is possible that liver tissue cuts with properties that are different from the gut tube, but these effects would appear more randomly, rather than as ordered structures. While the tissues were cleared before sectioning, this does not explain the effects we observed. Overall, we are comfortable that the findings that we observed are likely to be real. A good illustration of the high spatial resolution of the technique is the imaging of the E10 mouse liver (**Figure 2B, Figure 3F-3H**). It is very clear that these images are not due to artifacts.

One of the major weaknesses of our study was that there was only n=1 mouse and n = 1 human for each time point analyzed for the 3D reconstruction of embryonic stages of liver bud development. This can only be improved by expanding the data set, which was outside of the scope of this study. The mouse databases we used each have between 1-4 mice for each condition tested, but only 1 data set per time point is available for download. The number of slides is publicly available on the EMAP and 3D Embryo Atlas websites. We addressed this problem by obtaining tens to hundreds of other data points that have been obtained at later times of mouse development with imaging modalities and/or with liver weight data. We employed mouse imaging data from CT, MRI, optical projection tomography, and ultrasound. It is important to note that MRI data at E9.5 was likely overestimated because we were unable to distinguish between liver bud epithelium and STM. In fact, 6 of the 9 MRI-measured liver volumes were higher than the 3D reconstructued volumes from tissue sections, but the trends that we measured were similar. The only other technique to get more reliable and quantitative measurement is by noninvasive imaging of the intact embryo ex vivo or in vivo. However, any removal of the liver bud would essentially destroy it. The problems with ex vivo imaging, assuming the embryo is no longer alive, is that embryo tissues will have lost tension, as well as blood flow, and organs will lose shape. Further,

depending on the imaging technique, there can be many confounding factors to getting the high resolution images we have obtained and analyzed, and very likely the liver bud would lose any sources of potential contrast. The problem with in vivo imaging as the only option is that there will be motion artifact, due to both the mother and the embryo, which will cause a loss of spatial resolution, and more confounding layers like extraembryonic tissues (yolk sac) and structure(umbilical vein), that will cause most imaging techniques to lose considerable spatial resolution. Therefore, there cannot be a more quantitative and reliable technique, at a higher resolution, provided our tracing of the organ was accurate, using any existing imaging technology or technique. It is important to note that our approach was validated by our Gompertizan curve fits, which predict rapidly growing tissue initially, which also agrees with our manual measurements of data present in mouse atlas. A final limitation of the study is the relative assignment of pixels towards one versus another tissue group. We carefully reviewed the literature to make evidence-based predictions about the spatiotemporal location of the respective tissues, segmented by color. The gut tube was highlighted in yellow, the liver diverticulum as an outpocketing of the gut tube was highlighted in green. The STM of the liver bud was then highlighted in red. We acknowledge that there could be minor errors using this approach and that more exact methods could be used to confirm these results. However, these errors would not explain the regular structures that we observe and would only contribute minor errors to our volume calculations without changing the trends observed.

CONCLUSION

In conclusion, we have identified new aspects of liver growth, liver morphogenesis, and interactions between liver epithelium and STM. Newer techniques can be employed, like CT, MRI, photoacoustic imaging, and optical projection imaging, to improve datasets, and coupling 3D anatomical information to molecular information like gene expression, could be performed using techniques liked expansion microscopy (Chen, Tillberg et al. 2015). Another approach to understand these morphogenetic steps is whole embryo culture at the earliest stages. Overall, we feel understanding and imaging 3D these processes may lead to further insights about how the liver manages to greatly expand its mass while establishing an underlying complex architecture.

Table I: Total mouse number obtained from imaging modalities and liver weights.

dpc	Total mouse number at each time	Total mouse number from imaging data	Mouse number from micro-CT	Mouse number from MRI	Mouse number from tissue section	Mouse number from optical projection imaging	Mouse number from liver weight data
E8.5 dpc	1	1	0	0	1	0	0
E9.0 dpc	1	1	0	0	1	0	0
E9.5 dpc	3	3	0	2	1	0	0
E10 dpc	2	2	0	1	1	0	0
E10.5 dpc	3	3	0	1	2	0	0
E11 dpc	2	2	0	1	1	0	0
E11.5 dpc	3	3	0	1	1	1	0
E12 dpc	2	2	0	0	1	1	0
E13 dpc	32	2	0	0	1	1	30
E14 dpc	13	3	0	1	1	1	10
E14.5 dpc	11	0	0	0	0	0	11
E15 dpc	10	0	0	0	0	0	10
E15.5 dpc	35	35	35	0	0	0	0
E16 dpc	10	0	0	0	0	0	10
E18 dpc	12	2	2	1	1	0	10

Table II. Voxel size information for each mouse data set.

Name	Voxel X (micron)	Voxel Y (micron)	Voxel Z (micron)
E8.5 H&E Stain (EMA13)	4	4	4
E9.0 H&E Stain (EMA14)	4	4	7
E9.5 H&E Stain (EMA28)	4	4	7
E10 H&E Stain (EMA38)	4	4	7
E10.5 H&E Stain (EMA48)	4	4	7
E10.5 H&E Stain (EMA49)	4	4	7
E11 H&E Stain (EMA54)	4	4	7
E11.5 H&E Stain (EMA65)	4	4	7
E12 H&E Stain (EMA76)	4	4	7
E13 H&E Stain (EMA78)	16.5	16.5	16.5
E14 H&E Stain (EMA79)	4	4	7
E18 H&E Stain (EMA102)	13.3	13.3	14
E9.5 MRI (EMA36)	6.2	6.2	6.2
E9.5 MRI (EMA37)	8	8	8
E10 MRI (EMA47)	7.8	7.8	7.8
E10.5 MRI (EMA53)	8	8	8
E11 MRI (EMA64)	9.9	9.9	9.9
E11.5 MRI (EMA75)	11	11	11
E14 MRI	4.99	4.99	4.99
E18 MRI	4.71	4.71	4.71
E11.5, 12, 13, 14 Optical	17.66	17.66	17.66

Projection			
E15.5 Micron CT	27	27	27

Table III. Voxel size for human studies.

Day	**Voxel X (micron)**	**Voxel Y (micron)**	**Voxel Z (micron)**	**Number of Slices**
25	0.862	0.862	8.694	283
28	2.969	2.969	10.31	277
33	5.885	5.885	16.55	247
37	10.1209	10.1155	10.06	651
41	5.2600	5.2600	20.00	547
44	4.4790	4.4790	10.00	1059
52	4.4800	4.4800	60.00	288
56	24.8004	24.8004	144.3	208

Table IV: Estimation of liver cell density.

Embryo development stage (dpc)	**Estimated cell count assuming cell size of 1000µm^3**	**Estimate cell count assuming density of adult liver**
8.5	347	42
9	1404	168
9.5	2799	336
10	5806	697
10.5	36762	4411
11	66884	8026
11.5	246807	29617
12	385093	46211
13	4219793	506375
14	15645540	1877465
15.5	35600215	2639455
18	21995459	4272026

Table V: Liver Volume Estimation.

Embryo development stage (dpc)	Liver Volume (cm^3)	Normalized Liver Volume
8.5	346944	1
9	1403808	4.046209186
9.5	1396752	4.02587161
9.5	2939537	8.472655529
9.5	4059648	11.70116215
10	4357696	12.56022874
10	7255136	20.91154768
10.5	28412384	81.89328537
10.5	56539648	162.9647666
10.5	25333060	73.01772044
11	45120791	130.0520862
11	88646690	255.5072
11.5	172017664	495.8081535
11.5	178403247	514.2133803
11.5	390000000	1124.100719
12	267186976	770.1155691
12	503000000	1449.801697
13	5206585434	15006.99085
13	3233000000	9318.506733
14	10457620839	30142.10028
14	10757000000	31005.00369
14	25722000000	74138.76591
15.5	21995458967	63397.72115
15.5	25833171873	74459.19766
15.5	21221110003	61165.80775
15.5	21776170647	62765.66433
15.5	23398227120	67440.93318
18	30256430416	87208.39794
18	40944000000	118013.2817

ABBREVIATIONS

2D – two-dimensional

3D – three-dimensional

EMAP – emouse atlas project

STM – septum transversum mesenchyme

HEP – hepatocytes

FGF – fibroblast growth factor

BMP4 – bone morphogenetic protein 4

FOXA2 - forkhead box 2

Hex - homeobox protein

Prox1 – prospero homeobox 1

Tbx3 – T-box transcription box factor 3

EMT - epithelial to mesenchymal transition

TGFB – transforming growth factor beta

ARF6 - ADP-ribosylation factor 6

VEGF-A - vascular endothelial growth factor

HGF – hepatocyte growth factor

IL-6 – interleukin 6

HNF4a – hepatocyte nuclear factor 4 alpha

GATA6 – GATA Binding Protein 6

GATA4 – GATA Binding Protein 4

CT – computed tomography

MRI - magnetic resonance imaging

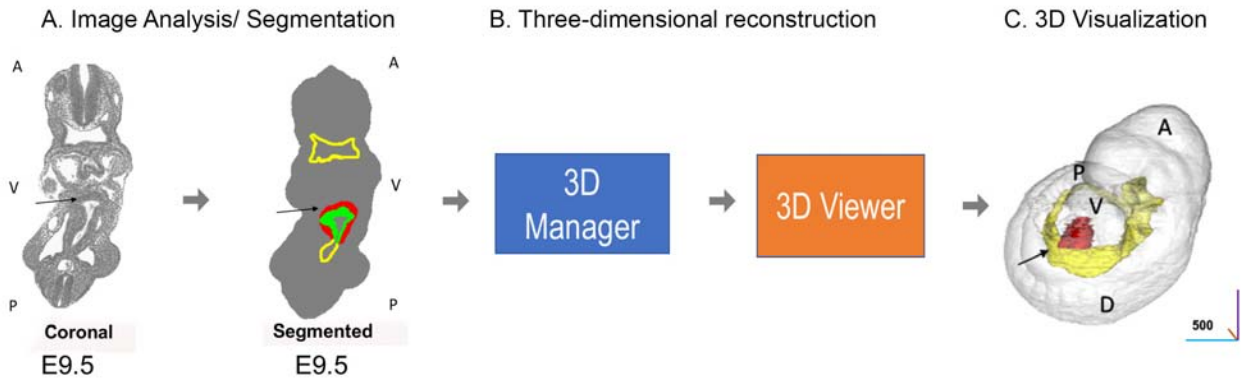

Figure 1. Figure 1. Data processing for 3D reconstruction of mouse liver bud. Listed are the steps in acquiring imaging data, segmenting data, and performing 3D reconstruction. 1) Access emouseatlas.org, mouse anatomy atlas, 2) Choose dataset and time point, 3) Click on download, obtain zip file wlz format of the embryo, 4) Download Woolz from EMAP/Analysis Tools & Resources/Software in the main menu bar 5) Use WlzExtFFConvert from the command line to convert wlz to nii format 6) Import nii format into ImageJ. A similar process was used for human liver as described in methods.

A) At this stage, a cleared, sectioned H & E stained embryo is visualized.The image is opened in "Segmentation Editor" and the key parts of the liver bud, mesenchyme, and gut tube are segmented using the mouse atlas with unique colors, using previous liver bud papers or mouse altals as a guide. The label file is saved.

B) The 3D Manger (plugin) is used to visualize 3D structure (3D Viewer) and 3D measure is used to perform analysis (i.e. volume).

C) 3D reconstruction is performed using 3D viewer with a smoothness factor of 10. Data was checked against mouse atlas and other studies of liver development to ensure accuracy. Scale bar unit is in microns.

FIGURES

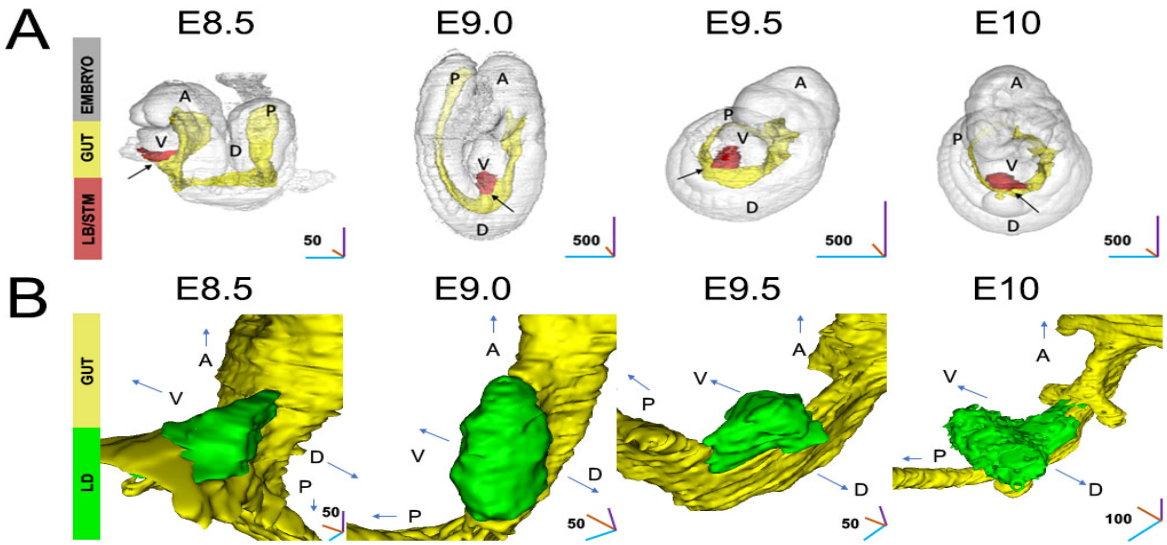

Figure 2. 3D reconstruction and visualization of the developing murine liver bud.

To dynamically visualize morphogenetic stages during mouse liver bud formation, 3D datasets, consisting of cleared hematoxylin and eosin (H& E) tissue sections from mouse development were used. Datasets were reformatted, imported, segmented, and reconstructed in 3D. Ventral views are shown. A = anterior, V = ventral, P = posterior. Arrows depict directions, gut tube (yellow), the liver bud (green). One specimen was used for each time point.

A) Whole body 3D reconstruction of the developing embryo at transient times of development (E8.5, E9.0, E9.5,E10). The major components of the murine liver bud are highlighted in separate colors. Gut tube (yellow), and Liver bud (LB) and septum transversum mesenchyme (STM) in red. Arrows (black) indicate location of the LB/STM. Scale bar in first panel is in µm. Scale bar in next three panels is in microns.

B) 3D reconstruction of the posterior foregut focused on the liver murine liver bud, at E8.5 from Theiler Stage (TS) 13. Liver epithelium initially appears as a triangular sheet of cells with a base of 25 µm At E9.0 (TS14)gut tube has closed with the liver bud, forming an elliptical shape tube-like structure with long axis in the cranial-caudal direction. For E9.5 (TS15) the liver bud remodels its shape, with an elliptical long axis in the lateral direction. At E10.0 (TS16). Liver bud remodeling with an elliptical long axis extending bi-laterally. At this stage, the axis has completely changed from E9.0. The liver surface appears more roughened.

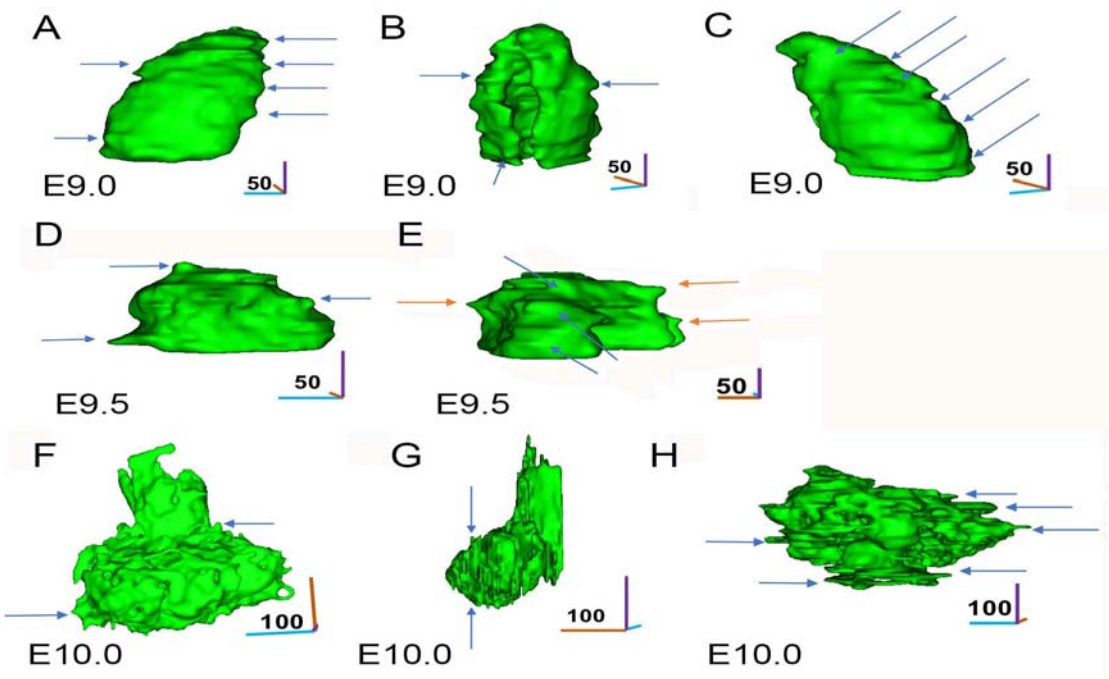

Figure 3. Multiple views of 3D murine liver bud demonstrate dynamic formation of cord-like structures and sheet-like growth.

To further image detailed morphogenetic structures, the surrounding structures were removed and only the liver bud was visualized in 3D. This enables the detailed visualization of the 3D morphogenetic features of hepatic cords, which are normally viewed only in 2D sections. Arrows below depict examples of migrating cords at different stages of development of sheet-like growth. Liver bud is depicted in green. One specimen was used per time point.

A) 3D reconstruction of the 9.0 murine liver bud, ventral view. Arrows demonstrate multiple early hepatic cords which demonstrate migration in the lateral directions.
B) Same as A), except dorsal view. The dorsal view demonstrates how the liver bud wraps around the gut tissue (which is absent), with an associated lumen. The associated hepatic cords are depicted by arrows.
C) Same as B), except right lateral view. In this case, arrows depict not hepatic cords, but sheet-like growth at various levels in the cranial-caudal axis. This sheet-like growth appears most prominently in this view.
D) 3D reconstruction of the E9.5 murine liver bud (TS15), inferior view. Blue arrows depict hepatic cords, while sheet-like growth is not observed.
E) Same protrusion structure as D), except left lateral view. Blue arrows depict hepatic cords, while orange arrows depict sheet-like growth.
F) 3D reconstruction of the E10.0 murine liver bud (TS16). Arrows depict examples of migrating cords. The liver bud now demonstrates a trabeculated tissue with interconnecting open-spaces.
G) Same protrusion structure as C), except left lateral view, demonstrating trabeculated tissue. Arrows depict potential hepatic cords.
H) Same protrusion structure as C), except inferior view, demonstrating trabeculated tissue. Arrows depict potential hepatic cords.

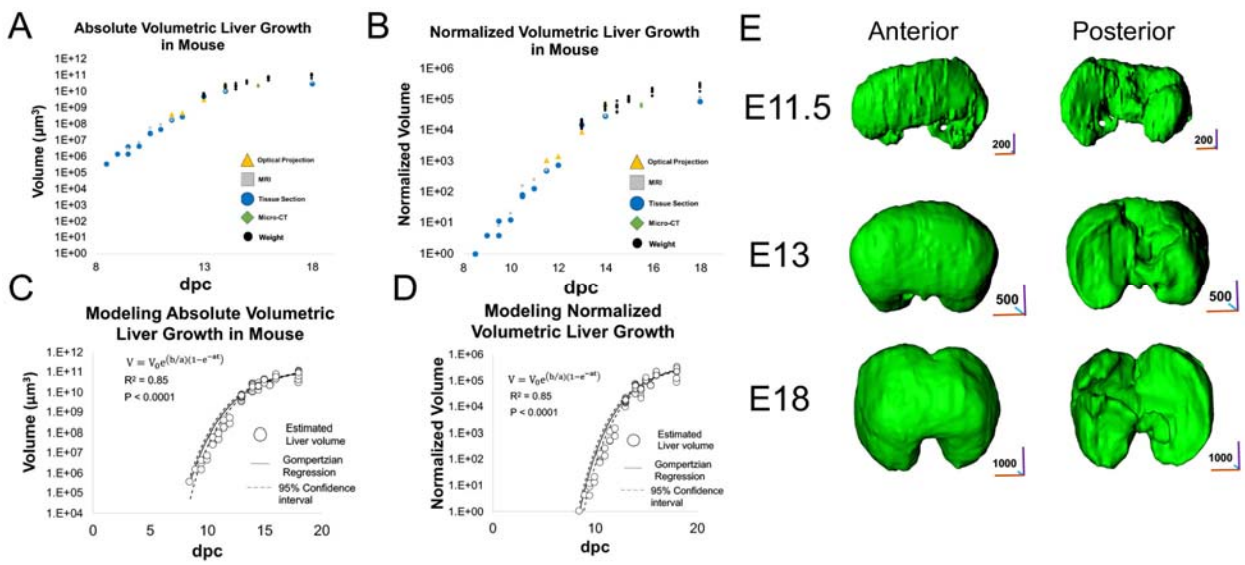

Figure 4. Quantification of the volumetric growth of the murine developing liver. Since images demonstrated rapid liver bud growth, volumetric growth was quantified from E8.5-11.5 (embryonic stage) and E12-18 (fetal liver stage). Volumetric data was obtained from 3D reconstruction of tissue slices, MRI, optical projection imaging and liver weights. E8.5-E18 (n=1, E8.5; n=1, E9; n=3, E9.5; n=2, E10; n=3, E10.5, n=2, E11, n=3, E11.5; n=2, E12; n=32, E13; n=13, E14; n=11, E14.5; n=10, E15; n=35, E15.5; n=10, E16; n=12, E18). An observed 10^5-fold increase in liver volume from E8.5 to E18.

A) Absolute volume of the reconstructed 3D liver murine liver. Plotted points are identified in different colors based on source of data: optical projection (yellow), magnetic resonance imaging (gray), tissue section (blue), micro-CT (green) and liver weight (black).

B) Relative liver volume was calculated by normalizing to the liver embryo volume at E8.5. Plotted points are identified in different colors based on source of data: optical projection (yellow), magnetic resonance imaging (gray), tissue section (blue), micro-CT (green) and liver weight (black).

C) Absolute liver volume changes are modeled using a non-linear regression Gompertzian model of tissue growth and fitted to the equation $V = V_o e^{\frac{b}{a}*(1-e^{-at})}$. Assuming 95% confidence interval), V_o=1.0E-72; a = 0.3069, 0.3245; and b = 58.16, 61.40; RMSE = 11,418,126,684. R^2 = 0.85, and P < 0.001.

D) Relative liver volume was calculated by normalizing to the corresponding embryo volume. Changes are modelled using a non-linear regression Gompertzian model of tissue growth and

fitted to the equation $V = V_0 e^{\frac{b}{a}*(1-e^{-at})}$. Assuming 95% confidence interval, V_0=2.9E-78, a = 0.3069, 0.3245; and b = 58.16, 61.40; RMSE = 32911. R^2 = 0.85 and P < 0.001.

E) 3D reconstruction of the liver bud at E11.5, E13, and E18 (green). Anterior and posterior views of the developing liver.

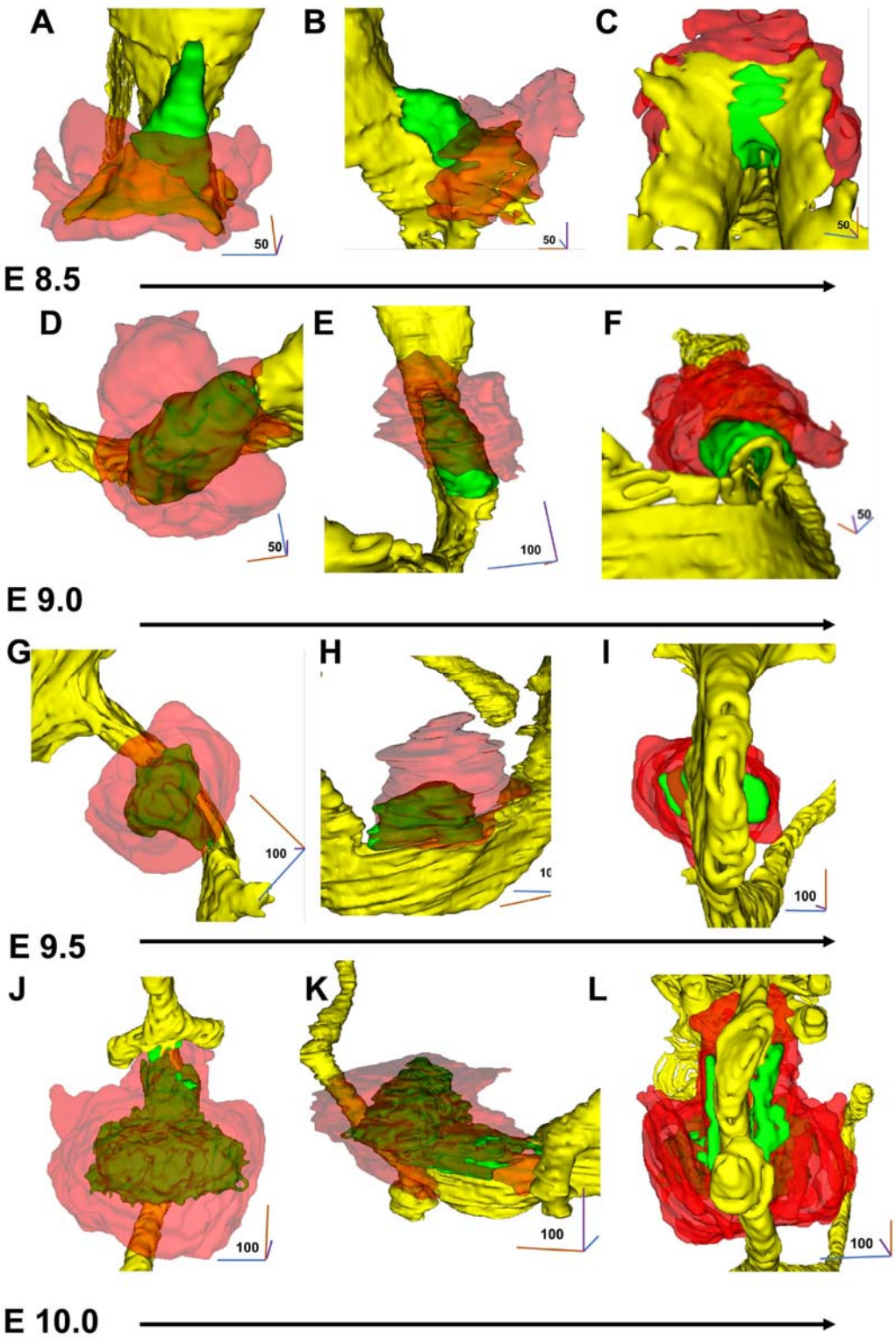
A
B
C
E 8.5
D
E
F
E 9.0
G
H
I
E 9.5
J
K
L
E 10.0

Figure 5. Visualization of 3D reconstructed murine liver bud and septum transversum mesenchyme (STM) interactions.

The STM has a key role in liver development. To visualize liver bud-STM interactions during early liver bud morphogenesis, the liver bud, the gut tube, and the STM were visualized together during early liver bud development. This was performed as described in Figure 1. Each time point based on one specimen.

A) 3D reconstruction of the liver murine liver bud and STM, at E8.5. Ventral view. Liver bud (green), STM (red). Visualization of the STM at E8.5 demonstrates that it covers the inferior ~ ½ of the E8.5 liver bud.

B) Same as A) except right lateral view. The STM extends ventrally for a distance similar to the dorsal-ventral thickness of the liver bud.

C) Same as A) except inferior view. The width of the STM in the lateral direction is about ¾ of the lateral thickness of the liver bud.

D) 3D reconstruction of the liver murine liver bud and STM, at E9.0 Superior, ventral, lateral view. the STM extends laterally for a length equal to ¾ times the lateral (smaller) diameter, and covers approximately 80% of the liver bud.

E) Same as D) except ventral, right lateral view, demonstrating the STM extends laterally for a length equal to ¾ times the lateral (smaller) diameter, and covers approximately 80% of the liver bud.

F) Same as E) except ventral, inferior (caudal) view. This demonstrates how the STM contacts the liver bud directly.

G) 3D reconstruction of the liver murine liver bud and septum transversum mesenchyme, at E9.5 Ventral, lateral view. The STM extends laterally about ½ times the diameter of the liver bud, and fully surrounds the liver bud. This suggests that the STM grows, remodels with the liver bud, and potentially primes the liver for growth.

H) Same as G) except right lateral view. The STM appears to be as thick as the liver bud when viewed laterally.

I) Same as G) except dorsal view. The STM extends laterally, for a distance of 1/3 times the lateral width of the liver bud.

J) 3D reconstruction of the liver murine liver bud and STM, at E10.0 Ventral, lateral view. Compared to E9.5, the lateral STM thickness has increased.

K) Same as J) except left lateral view. The STM has diminished in the ventral direction.

L) Same as J) except posterior view. The STM has diminished in the lateral direction.

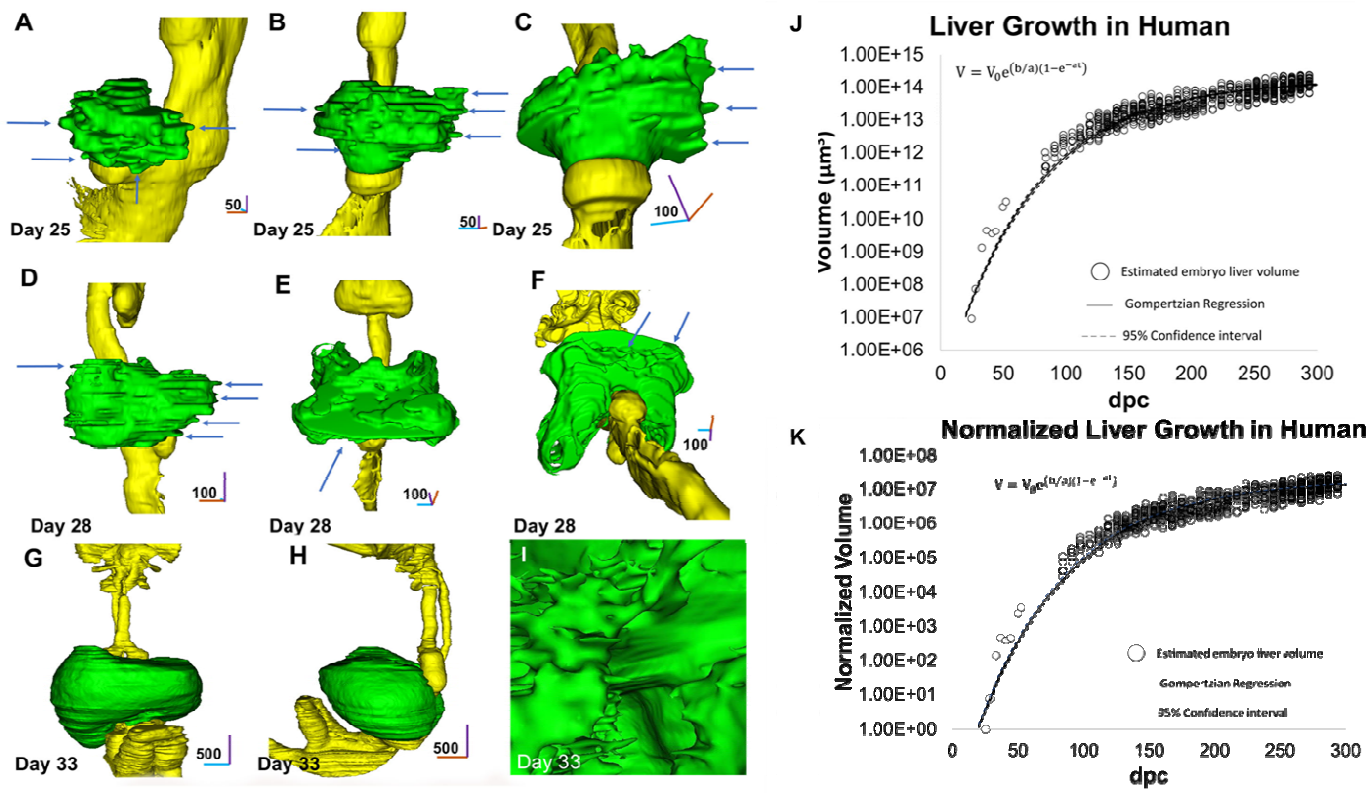

Figure 6. 3D reconstruction and visualization of the developing human liver bud.
To understand dynamics of liver bud morphogenesis, the human liver bud was imaged in 3D similar to the procedure used to visualize the mouse liver bud. 3D datasets, consisting of cleared hematoxylin and eosin (H&E) tissue sections from the 3D Atlas of Human Embryology were used. Datasets were reformatted, imported, segmented, and reconstructed in 3D. Ventral views are shown. Each time point based on one specimen. Gut tube (yellow), the liver bud (green). Sample per timepoint are n=9, Days 25-56, n = 930, Day 125 - 294
A) 3D reconstruction of the human liver bud on day 25. Arrows demonstrate hepatic cords (arrows), and sheet-like growth appears
B) Same as A) except ventral view. Lateral hepatic cords (arrows) can be visualized, and sheet-like growth is again observed.
C) Same as A) except, inferior, left lateral, ventral view. Lateral hepatic cords can be visualized (arrows), and inferior view enables observation of sheet like growth. In some cases, sheets of cells are bounded by hepatic cords. Layers of sheets can be clearly visualized.
D) 3D reconstruction focused of the human liver bud on day 28. Lateral view. Arrows depict migrating cords. Although larger than day 25, the liver bud demonstrates sheet-like growth and hepatic cords.
E) Same as D) except anterior, dorsal view. Arrow depicts tissue which wraps around anatomical structures. Dorsal side does not demonstrate appreciable hepatic cords.
F) Same as D) except ventral view. Arrows depicting sheet of migrating cells extending medially and laterally.
G) 3D reconstruction focused of the human liver bud on day 33. Ventral view. Image demonstrates that the liver has enlarged and is smoothened, with no hepatic cords or cell sheets are present.
H) Same as G) except lateral view. Again, no hepatic cords or hepatic sheets are present. Inside view of the 3D reconstruction focused of the human liver bud on day 33.
I) The green images demonstrate numerous enclosed green structures and trabeculation, all of which are in fact empty spaces within the 3D constructed liver. Interconnections can be seen inside the liver as the green portions are enclosed voids.
J) Absolute human liver volume changes are modelled using a non-linear regression Gompertzian model of tissue growth and fitted to the equation $V = V_0 e^{(b/a)(1-e^{-at})}$. Assuming 95% confidence interval, whereby V_0 =50,000, a = 0.014, 0.015; b = 0.31, 0.33; $P < 0.001$, $R^2 = 0.84$ and RMSE = 3,087,758.
K) Relative human liver volume was calculated by normalizing to the embryo liver volume at day 25. Changes are modeled using a non-linear regression Gompertzian model of tissue growth and fitted to the equation $V = V_0 e^{(b/a)(1-e^{-at})}$. Assuming 95% confidence interval, whereby V_0 =0.0056, a = 0.014, 0.015; b = 0.31, 0.33; $P < 0.001$, $R^2 = 0.84$ and RMSE = 1037.

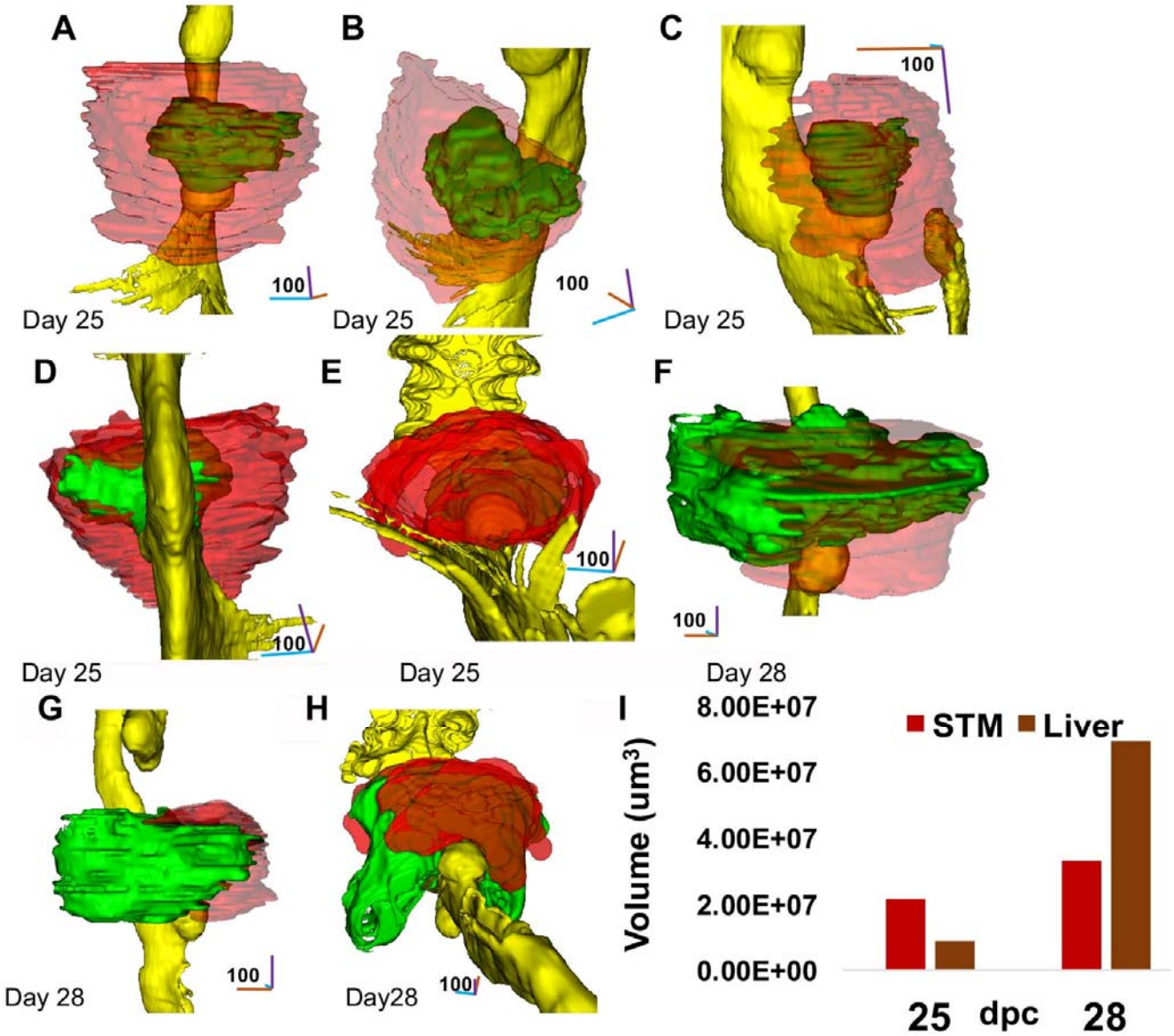

Figure 7. Visualization of 3D reconstructed human liver bud and septum transversum mesenchyme (STM) interactions.

To understand the role of the STM in human liver bud morphogenesis, human liver bud was again imaged in 3D as in Figure 6, except the STM was added to the images. 3D datasets, consisting of cleared hematoxylin and eosin (H&E) tissue sections from the 3D Atlas of Human Embryology were used. Datasets were reformatted, imported, segmented, and reconstructed in 3D. Ventral views are shown. Each time point based on one specimen. Ventral, lateral view. The STM model was rendered at 50% transparency. Each time point based on one specimen.

A) 3D reconstruction of the human liver bud and STM, at Day 25. Ventral view. Liver bud (green), STM (red). At this stage, the STM completely envelops the liver. The human liver bud is surrounded by the STM, extending about ½ times the width and height of the liver bud. The posterior is not fully covered.

B) Same as A, except superior, lateral view. The STM continues to envelop the liver in all directions.
C) Same as A, except right, lateral view. The STM envelops the liver.
D) Same as D, except dorsal view. Portions of the liver bud are free from STM, in the posterior portion of liver bud.
E) Same as A, except inferior view. STM envelops the liver bud, and appears to form a tail-like structure inferiorly.
F) 3D reconstruction of the human liver bud and STM, at Day 28. Ventral, lateral view. The STM is observable superiorly and inferiorly, but within the sheet of cells within the center of the liver.
G) Same as F, except right, lateral view. STM is not observed at this stage.
H) Same as F, except inferior view with the ventral surface facing up. STM is not observed on the dorsal side of liver but is present on the ventral side.
I) Quantification of human STM and liver bud volume during human liver development on days 25 and 28. The liver growth, in terms of volume, has overtaken the STM by day 28, unlike the mouse.

SUPPLEMENTARY FIGURE LEGENDS

Supplemental Figure 1. Segmentation process of murine liver development in whole embryo at E8.5.

A) Coronal, black and white, hematoxylin and eosin (H+E) stain tissue section at E8.5 of mouse development, obtained from eMouseAtlas database, and corresponding segmented image. In segmented image, the gut tube (yellow), the liver bud (green) and STM (red) were segmented. A = Anterior, V = Ventral, P = Posterior, D= Dorsal. Arrows depict liver bud.

B) Same as A, except sagittal sections and corresponding segmented image.

Supplemental Figure 2. Dynamic 3D imaging of murine liver development in whole embryo.

A) Coronal, black and white, hematoxylin and eosin (H+E) stain tissue section at E9.0 of mouse development, obtained from eMouseAtlas database, and corresponding segmented image. In segmented image, the gut tube (yellow), the liver bud (green) and STM (red) were segmented. A = Anterior, V = Ventral, P = Posterior, D= Dorsal. Arrows depict liver bud.

B) Same as A, except sagittal sections and corresponding segmented image.

Supplemental Figure 3. Segmentation process of murine liver development in whole embryo at E9.0.

Same as Supplemental Figure 2 except E10.0. Scale bar is in microns.

Supplemental Figure 4. Segmentation process of murine liver development in whole embryo at E10.0.

3D reconstruction of the liver bud at E8.5, Transverse view. Scale bar is in microns.

Supplemental Figure 5. Quantification of septum transversum mesenchyme (STM) volume during murine liver development.

To measure the dynamics of STM growth, volumes were measured after loading segmented images of embryos. Relative volumes were normalized by taking the ratio to the corresponding embryo volumes. Each time point based on one specimen.

A) Ratio of the reconstructed 3D liver murine liver growth compared to the mouse embryo at E8.5-E10. STM growth mirrors the growth patterns of the liver bud.
B) Absolute volume of the reconstructed 3D liver murine liver growth at E8.5-E10. STM does not stay constant, but exhibits growth that patterns growth of the liver bud, including discontinuous growth.

Supplemental Figure 6. 3D reconstruction and visualization of human liver development in whole embryo.

A) Whole human embryo 3D reconstruction demonstrating reconstructed human embryo on Day 25. Each tissue of interest was identified and thresholded and traced on individual, transverse tissue slices using known cross sectional anatomy and pre-identified labels within the database. Gut tube (yellow), the liver bud (green) and STM (red). A = Anterior, V = Ventral, P = Posterior, D= Dorsal.
B) Same as A except Day 28 in human development.
C) Same as B except Day 33 in human development.

Supplemental Figure 7. Ventral view of human liver development at Day 33.

The liver bud (green) and gut tube (yellow) is viewed at the anterior position looking towards ventral. Scale in microns.

Supplemental Figure 8. Dorsal view of human liver development at Day 33.

Dorsal view of liver bud (green) and gut tube (yellow). Scale in microns.

Supplemental Video 1. Murine liver bud at E8.5 in 360° rotation through sagittal plane.

Ventral view of liver bud (green) rotating through sagittal plane. Units in axis are microns.

Supplemental Video 2. Murine liver bud at E9.0 in 360° rotation through sagittal plane.

Ventral view of liver bud (green) rotating through sagittal plane. Units in axis are microns.

Supplemental Video 3. Murine liver bud at E9.5 in 360° rotation through sagittal plane.

Ventral view of liver bud (green) rotating through sagittal plane. Units in axis are microns.

Supplemental Video 4. Murine liver bud at E10.0 in 360° rotation through sagittal plane.

Ventral view of liver bud (green) rotating through sagittal plane. Units in axis are microns.

Supplemental Video 5. Interior view of murine liver bud at E10.0.

Interior view of liver bud (green) through sagittal plane. Interior view is inverted as the structures (green) are voids within the liver bud and empty space is where the liver bud is solid. Units in axis are microns.

Supplemental Video 6. Murine liver bud and STM at E8.5 in 360° rotation through sagittal plane.

Ventral view of liver bud (green) and STM (red) rotating through sagittal plane. Units in axis are microns.

Supplemental Video 7. Murine liver bud and STM at E9.0 in 360° rotation through sagittal plane.

Ventral view of liver bud (green) and STM (red) rotating through sagittal plane. Units in axis are microns.

Supplemental Video 8. Murine liver bud and STM at E9.5 in 360° rotation through sagittal plane.

Ventral view of liver bud (green) and STM (red) rotating through sagittal plane. Units in axis are microns.

Supplemental Video 9. Murine liver bud and STM at E10.0 in 360° rotation through sagittal plane.

Ventral view of liver bud (green) and STM (red) rotating through sagittal plane. Units in axis are microns.

Supplemental Video 10. Human liver bud at Day 25 in 360° rotation through sagittal plane.

Ventral view of liver bud (green) rotating through sagittal plane. Units in axis are microns.

Supplemental Video 11. Human liver bud at Day 25 in 360° rotation through sagittal plane.

Ventral view of liver bud (green) rotating through transverse plane. Units in axis are microns.

Supplemental Video 12. Human liver bud at Day 28 in 360° rotation through sagittal plane.

Ventral view of liver bud (green) rotating through sagittal plane. Units in axis are microns.

Supplemental Video 13. Human liver bud at Day 28 in 360° rotation through sagittal plane.

Ventral view of liver bud (green) rotating through transverse plane. Units in axis are microns.

Supplemental Video 14. Human liver bud at Day 33 in 360° rotation through sagittal plane.

Ventral view of liver bud (green) rotating through sagittal plane. Units in axis are microns.

Supplemental Video. 15. Human liver bud at Day 33 in 360° rotation through sagittal plane.

Ventral view of liver bud (green) rotating through transverse plane. Units in axis are microns.

Supplemental Video 16. Interior view of human liver bud at day 33.

Interior view of liver bud (green) through sagittal plane. Interior view is inverted as the structures (green) are voids within the liver bud and empty space is where the liver bud is solid. Units in axis are microns.

Supplemental Video 17. Human liver bud and STM at Day 25 in 360° rotation through sagittal plane.

Ventral view of liver bud (green) and STM (red) rotating through sagittal plane. Units in axis are microns.

Supplemental Video 18. Human liver bud and STM at Day 25 in 360° rotation through sagittal plane.

Ventral view of liver bud (green) and STM (red) rotating through transverse plane. Units in axis are microns.

Supplemental Video 19. Human liver bud and STM at Day 28 in 360° rotation through sagittal plane.

Ventral view of liver bud (green) and STM (red) rotating through sagittal plane. Units in axis are microns.

Supplemental Video 20. Human liver bud and STM at Day 28 in 360° rotation through sagittal plane.

Ventral view of liver bud (green) and STM (red) rotating through transverse plane. Units in axis are microns.

ETHICS APPROVAL AND CONSENT TO PARTICIPATE

Not applicable.

CONSENT FOR PUBLICATION

Not applicable.

AVAILABILITY OF DATA AND MATERIALS

All data generated or analyzed during this study are included in this published article and its supplementary files.

COMPETING INTERESTS

The authors declare that they have no competing interests

FUNDING

NP was supported by University at Buffalo, School of Engineering, State University of NY startup funds and University at Buffalo, State University of NY, Stem cells and Regenerative Medicine program (ScIRM)", (New York Stem Cell Science NYSTEM (Contract #C30290GG). OO was supported by the Western New York Prosperity Fellowship.

AUTHOR CONTRIBUTIONS:

TM: Obtained data, analyzed data, developed methodology for acquisition and analysis, wrote and approved manuscript.

OO: Obtained data, analyzed data, wrote and approved manuscript.

DG: Obtained data, analyzed data, wrote and approved manuscript.

CS: Obtained data, analyzed data, approved manuscript

SR: Obtained data, analyzed data, approved manuscript

SR: Obtained data, analyzed data, approved manuscript

NP: Conceptualized, acquired funding, investigated, supervised, wrote, edited manuscript, and approved manuscript.

ACKNOWLEDGEMENTS:

We thank Dr. Duncan Davidson and Professor Richard Baldock for their efforts in developing the eMouseAtlas Project which provided the datasets we used to perform our embryological analysis. We thank Professor R. Mark Henkelman, Dr. Jason P. Lerch, Dr. Brian J. Nieman, and Dr. John G. Sled for their work as part of the Mouse Imaging Centre and for providing us with additional image data sets for mouse development. We also like to thank Professor Bernadette S. de Bakker and the rest of the 3D Atlas team for providing us with human embryo data sets.

.

REFERENCES

Baldock, R., J. Bard, M. Kaufman and D. Davidson (1992). "A real mouse for your computer." Bioessays **14**(7): 501-502.

Bin, W. T., L. M. Ma, Q. Xu and X. L. Shi (2012). "Embryonic hepatocyte transplantation for hepatic cirrhosis: efficacy and mechanism of action." World J Gastroenterol **18**(4): 309-322.

Bort, R., M. Signore, K. Tremblay, J. P. M. Barbera and K. S. Zaret (2006). "Hex homeobox gene controls the transition of the endoderm to a pseudostratified, cell emergent epithelium for liver bud development." Developmental Biology **290**(1): 44-56.

Bort, R., M. Signore, K. Tremblay, J. P. Martinez Barbera and K. S. Zaret (2006). "Hex homeobox gene controls the transition of the endoderm to a pseudostratified, cell emergent epithelium for liver bud development." Dev Biol **290**(1): 44-56.

Boylan, J. M., H. Francois-Vaughan, P. A. Gruppuso and J. A. Sanders (2017). "Engraftment and Repopulation Potential of Late Gestation Fetal Rat Hepatocytes." Transplantation **101**(10): 2349-2359.

Cascio, S. and K. S. Zaret (1991). "Hepatocyte differentiation initiates during endodermal-mesenchymal interactions prior to liver formation." Development **113**(1): 217-225.

Cayuso, J., A. Dzementsei, J. C. Fischer, G. Karemore, S. Caviglia, J. Bartholdson, G. J. Wright and E. A. Ober (2016). "EphrinB1/EphB3b Coordinate Bidirectional Epithelial-Mesenchymal Interactions Controlling Liver Morphogenesis and Laterality." Dev Cell **39**(3): 316-328.

Chen, F., P. W. Tillberg and E. S. Boyden (2015). "Optical imaging. Expansion microscopy." Science **347**(6221): 543-548.

Collardeau-Frachon, S. and J. Y. Scoazec (2008). "Vascular development and differentiation during human liver organogenesis." Anat Rec (Hoboken) **291**(6): 614-627.

Dabeva, M. D., P. M. Petkov, J. Sandhu, R. Oren, E. Laconi, E. Hurston and D. A. Shafritz (2000). "Proliferation and differentiation of fetal liver epithelial progenitor cells after transplantation into adult rat liver." Am J Pathol **156**(6): 2017-2031.

de Bakker, B. S., K. H. de Jong, J. Hagoort, K. de Bree, C. T. Besselink, F. E. de Kanter, T. Veldhuis, B. Bais, R. Schildmeijer, J. M. Ruijter, R. J. Oostra, V. M. Christoffels and A. F. Moorman (2016). "An interactive three-dimensional digital atlas and quantitative database of human development." Science **354**(6315).

de Bakker, B. S., K. H. de Jong, J. Hagoort, R. J. Oostra and A. F. Moorman (2012). "Towards a 3-dimensional atlas of the developing human embryo: the Amsterdam experience." Reprod Toxicol **34**(2): 225-236.

Enzan, H., H. Himeno, M. Hiroi, H. Kiyoku, T. Saibara and S. Onishi (1997). "Development of hepatic sinusoidal structure with special reference to the Ito cells." Microsc Res Tech **39**(4): 336-349.

Gordillo, M., T. Evans and V. Gouon-Evans (2015). "Orchestrating liver development." Development **142**(12): 2094-2108.

Hussain, S. Z., T. Sneddon, X. Tan, A. Micsenyi, G. K. Michalopoulos and S. P. Monga (2004). "Wnt impacts growth and differentiation in ex vivo liver development." Exp Cell Res **292**(1): 157-169.
Kamei, Y., O. Tsutsumi, A. Yamakawa, Y. Oka, Y. Taketani and J. Imaki (1999). "Maternal Epidermal Growth Factor Deficiency Causes Fetal Hypoglycemia and Intrauterine Growth Retardation in Mice: Possible Involvement of Placental Glucose Transporter GLUT3 Expression1." Endocrinology **140**(9): 4236-4243.
Kamiya, A., T. Kinoshita, Y. Ito, T. Matsui, Y. Morikawa, E. Senba, K. Nakashima, T. Taga, K. Yoshida, T. Kishimoto and A. Miyajima (1999). "Fetal liver development requires a paracrine action of oncostatin M through the gp130 signal transducer." EMBO J **18**(8): 2127-2136.
Koike, H., K. Iwasawa, R. Ouchi, M. Maezawa, K. Giesbrecht, N. Saiki, A. Ferguson, M. Kimura, W. L. Thompson, J. M. Wells, A. M. Zorn and T. Takebe (2019). "Modelling human hepato-biliary-pancreatic organogenesis from the foregut-midgut boundary." Nature **574**(7776): 112-116.
LeCouter, J., D. R. Moritz, B. Li, G. L. Phillips, X. H. Liang, H. P. Gerber, K. J. Hillan and N. Ferrara (2003). "Angiogenesis-independent endothelial protection of liver: role of VEGFR-1." Science **299**(5608): 890-893.
Ledouarin, N. (1963). "[Early Inductive Action of Mesoderm of the Cardiac Area on Hepatic Endoderm of the Chick Embryo]." C R Hebd Seances Acad Sci **257**: 1357-1360.
Lee, C. S., J. R. Friedman, J. T. Fulmer and K. H. Kaestner (2005). "The initiation of liver development is dependent on Foxa transcription factors." Nature **435**(7044): 944-947.
Lickert, H., J. K. Takeuchi, I. Von Both, J. R. Walls, F. McAuliffe, S. L. Adamson, R. M. Henkelman, J. L. Wrana, J. Rossant and B. G. Bruneau (2004). "Baf60c is essential for function of BAF chromatin remodelling complexes in heart development." Nature **432**(7013): 107-112.
Lints, T. J., L. Hartley, L. M. Parsons and R. P. Harvey (1996). "Mesoderm-specific expression of the divergent homeobox gene Hlx during murine embryogenesis." Dev Dyn **205**(4): 457-470.
Lotto, J., S. Drissler, R. Cullum, W. Wei, M. Setty, E. M. Bell, S. C. Boutet, S. Nowotschin, Y. Y. Kuo, V. Garg, D. Pe'er, D. M. Church, A. K. Hadjantonakis and P. A. Hoodless (2020). "Single-Cell Transcriptomics Reveals Early Emergence of Liver Parenchymal and Non-parenchymal Cell Lineages." Cell **183**(3): 702-716 e714.
Ludtke, T. H., V. M. Christoffels, M. Petry and A. Kispert (2009). "Tbx3 promotes liver bud expansion during mouse development by suppression of cholangiocyte differentiation." Hepatology **49**(3): 969-978.
Man, J., J. C. Hutchinson, M. Ashworth, I. Jeffrey, A. E. Heazell and N. J. Sebire (2016). "Organ weights and ratios for postmortem identification of fetal growth restriction: utility and confounding factors." Ultrasound Obstet Gynecol **48**(5): 585-590.
Margagliotti, S., F. Clotman, C. E. Pierreux, J. B. Beaudry, P. Jacquemin, G. G. Rousseau and F. P. Lemaigre (2007). "The Onecut transcription factors HNF-6/OC-1 and OC-2 regulate early liver expansion by controlling hepatoblast migration." Dev Biol **311**(2): 579-589.
Margagliotti, S., F. Clotman, C. E. Pierreux, P. Lemoine, G. G. Rousseau, P. Henriet and F. P. Lemaigre (2008). "Role of metalloproteinases at the onset of liver development." Dev Growth Differ **50**(5): 331-338.
Martinez Barbera, J. P., M. Clements, P. Thomas, T. Rodriguez, D. Meloy, D. Kioussis and R. S. Beddington (2000). "The homeobox gene Hex is required in definitive endodermal tissues for normal forebrain, liver and thyroid formation." Development **127**(11): 2433-2445.

Matsumoto, K., H. Yoshitomi, J. Rossant and K. S. Zaret (2001). "Liver organogenesis promoted by endothelial cells prior to vascular function." Science **294**(5542): 559-563.
Mehrara, E., E. Forssell-Aronsson, V. Johanson, L. Kolby, R. Hultborn and P. Bernhardt (2013). "A new method to estimate parameters of the growth model for metastatic tumours." Theor Biol Med Model **10**: 31.
Nieman, B. J., M. D. Wong and R. M. Henkelman (2011). "Genes into geometry: imaging for mouse development in 3D." Curr Opin Genet Dev **21**(5): 638-646.
Nomura, T. (1976). "Comparison of tumour susceptibility among various organs of foetal, young and adult ICR/Jcl mice." Br J Cancer **33**(5): 521-534.
Ober, E. A. and F. P. Lemaigre (2018). "Development of the liver: Insights into organ and tissue morphogenesis." J Hepatol **68**(5): 1049-1062.
Ogoke, O., J. Oluwole and N. Parashurama (2017). "Bioengineering considerations in liver regenerative medicine." J Biol Eng **11**: 46.
Pardi, G. and I. Cetin (2006). "Human fetal growth and organ development: 50 years of discoveries." Am J Obstet Gynecol **194**(4): 1088-1099.
Phoon, C. K. (2006). "Imaging tools for the developmental biologist: ultrasound biomicroscopy of mouse embryonic development." Pediatr Res **60**(1): 14-21.
Richardson, L., S. Venkataraman, P. Stevenson, Y. Yang, J. Moss, L. Graham, N. Burton, B. Hill, J. Rao, R. A. Baldock and C. Armit (2014). "EMAGE mouse embryo spatial gene expression database: 2014 update." Nucleic Acids Res **42**(Database issue): D835-844.
Rossi, J. M., N. R. Dunn, B. L. Hogan and K. S. Zaret (2001). "Distinct mesodermal signals, including BMPs from the septum transversum mesenchyme, are required in combination for hepatogenesis from the endoderm." Genes Dev **15**(15): 1998-2009.
Schmidt, C., F. Bladt, S. Goedecke, V. Brinkmann, W. Zschiesche, M. Sharpe, E. Gherardi and C. Birchmeier (1995). "Scatter factor/hepatocyte growth factor is essential for liver development." Nature **373**(6516): 699-702.
Semeraro, R., V. Cardinale, G. Carpino, R. Gentile, C. Napoli, R. Venere, M. Gatto, R. Brunelli, E. Gaudio and D. Alvaro (2013). "The fetal liver as cell source for the regenerative medicine of liver and pancreas." Ann Transl Med **1**(2): 13.
Sherwood, R. I., T. Y. Chen and D. A. Melton (2009). "Transcriptional dynamics of endodermal organ formation." Dev Dyn **238**(1): 29-42.
Si-Tayeb, K., F. P. Lemaigre and S. A. Duncan (2010). "Organogenesis and development of the liver." Dev Cell **18**(2): 175-189.
Song, H., J. Luo, W. Luo, J. Weng, Z. Wang, B. Li, D. Li and M. Liu (2008). "Inactivation of G-protein-coupled receptor 48 (Gpr48/Lgr4) impairs definitive erythropoiesis at midgestation through down-regulation of the ATF4 signaling pathway." J Biol Chem **283**(52): 36687-36697.
Sosa-Pineda, B., J. T. Wigle and G. Oliver (2000). "Hepatocyte migration during liver development requires Prox1." Nat Genet **25**(3): 254-255.
Suzuki, T., Y. Kanai, T. Hara, J. Sasaki, T. Sasaki, M. Kohara, T. Maehama, C. Taya, H. Shitara, H. Yonekawa, M. A. Frohman, T. Yokozeki and Y. Kanaho (2006). "Crucial role of the small GTPase ARF6 in hepatic cord formation during liver development." Mol Cell Biol **26**(16): 6149-6156.
Syed, S. H., K. V. Larin, M. E. Dickinson and I. V. Larina (2011). "Optical coherence tomography for high resolution imaging of mouse development in utero." J Biomed Opt **16**(4): 046004.

Szpinda, M., M. Paruszewska-Achtel, A. Wozniak, C. Mila-Kierzenkowska, G. Elminowska-Wenda, M. Dombek, A. Szpinda and M. Badura (2015). "Volumetric Growth of the Liver in the Human Fetus: An Anatomical, Hydrostatic, and Statistical Study." Biomed Res Int **2015**: 858162.
Tanimizu, N. and T. Mitaka (2017). "Epithelial Morphogenesis during Liver Development." Cold Spring Harb Perspect Biol **9**(8).
Tatsumi, N., R. Miki, K. Katsu and Y. Yokouchi (2007). "Neurturin-GFRalpha2 signaling controls liver bud migration along the ductus venosus in the chick embryo." Dev Biol **307**(1): 14-28.
Turnbull, D. H. and S. Mori (2007). "MRI in mouse developmental biology." NMR Biomed **20**(3): 265-274.
Udan, R. S., V. G. Piazza, C. W. Hsu, A. K. Hadjantonakis and M. E. Dickinson (2014). "Quantitative imaging of cell dynamics in mouse embryos using light-sheet microscopy." Development **141**(22): 4406-4414.
Watt, A. J., R. Zhao, J. Li and S. A. Duncan (2007). "Development of the mammalian liver and ventral pancreas is dependent on GATA4." BMC Dev Biol **7**: 37.
Weinstein, M., S. P. Monga, Y. Liu, S. G. Brodie, Y. Tang, C. Li, L. Mishra and C. X. Deng (2001). "Smad proteins and hepatocyte growth factor control parallel regulatory pathways that converge on beta1-integrin to promote normal liver development." Mol Cell Biol **21**(15): 5122-5131.
Wong, M. D., M. C. van Eede, S. Spring, S. Jevtic, J. C. Boughner, J. P. Lerch and R. M. Henkelman (2015). "4D atlas of the mouse embryo for precise morphological staging." Development **142**(20): 3583-3591.
Yagi, H., K. Deguchi, A. Aono, Y. Tani, T. Kishimoto and T. Komori (1998). "Growth disturbance in fetal liver hematopoiesis of Mll-mutant mice." Blood **92**(1): 108-117.
Yang, D., P. Gao, C. Tian and Y. Sheng (2020). "Gompertz tracking of the growth trajectories of the human-liver-cancer xenograft-tumors in nude mice." Comput Methods Programs Biomed **191**: 105412.
Yoshimura, A., M. Ichihara, I. Kinjyo, M. Moriyama, N. G. Copeland, D. J. Gilbert, N. A. Jenkins, T. Hara and A. Miyajima (1996). "Mouse oncostatin M: an immediate early gene induced by multiple cytokines through the JAK-STAT5 pathway." EMBO J **15**(5): 1055-1063.
Zhao, R., A. J. Watt, J. Li, J. Luebke-Wheeler, E. E. Morrisey and S. A. Duncan (2005). "GATA6 is essential for embryonic development of the liver but dispensable for early heart formation." Mol Cell Biol **25**(7): 2622-2631.
Zorn, A. M. (2008). Liver development. StemBook. Cambridge (MA).

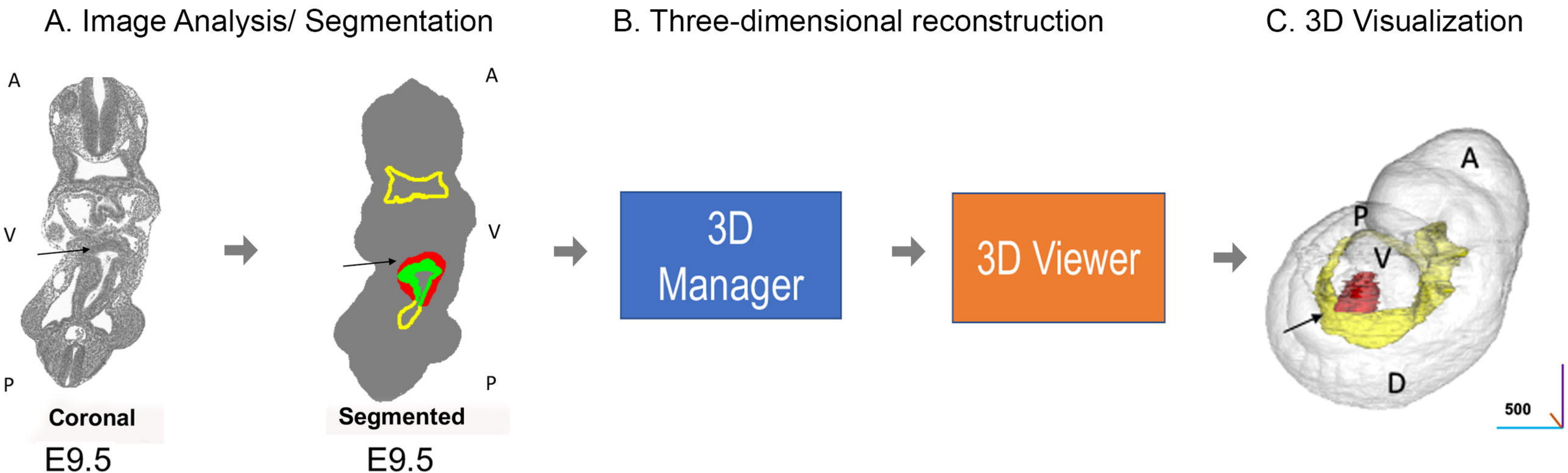
A. Image Analysis/ Segmentation
B. Three-dimensional reconstruction
C. 3D Visualization
A
V
P
Coronal
E9.5
A
V
P
Segmented
E9.5
3D Manager
3D Viewer
A
P
V
D
500

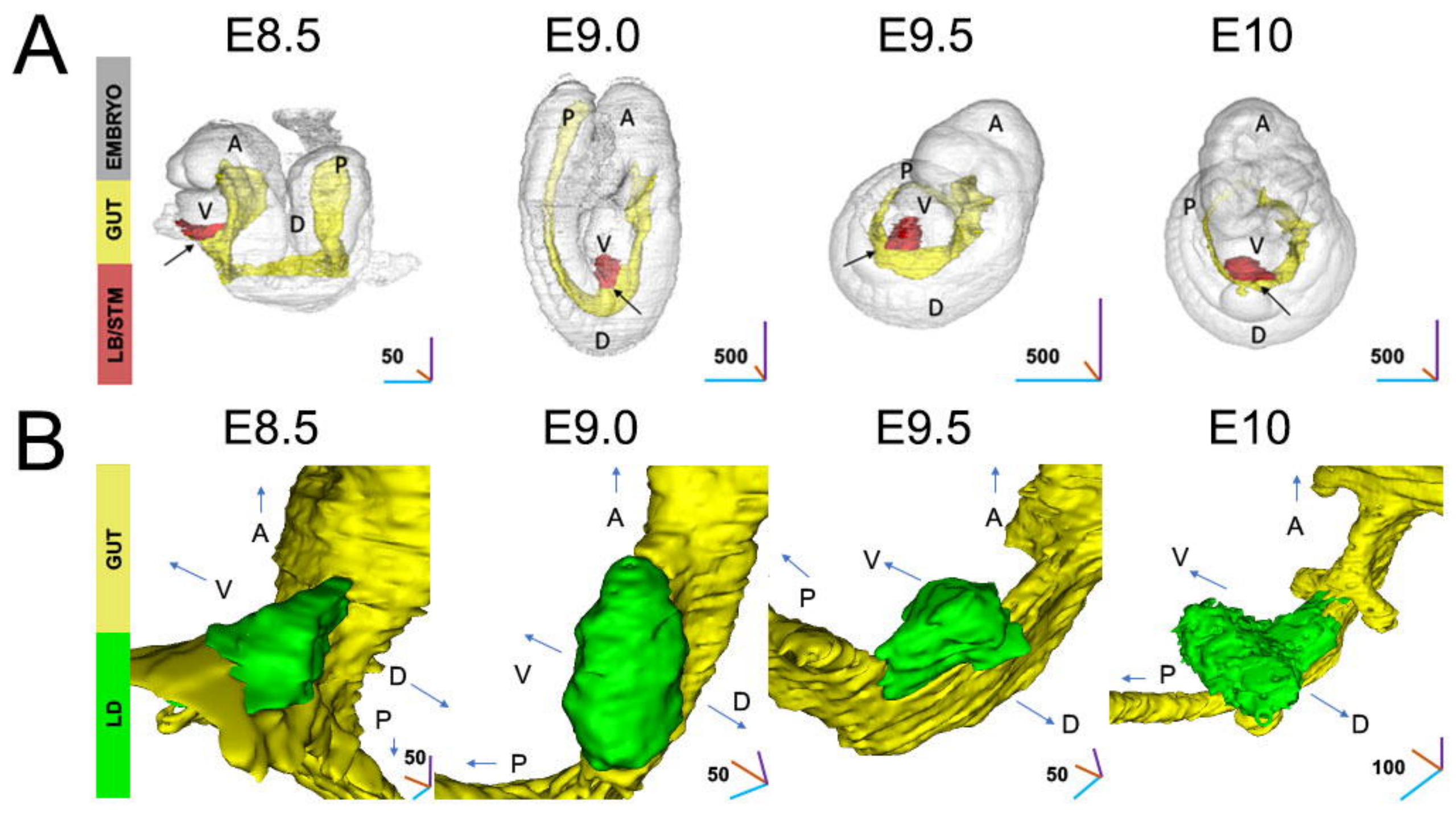
A
E8.5
E9.0
E9.5
E10
EMBRYO
GUT
LB/STM
A
P
V
D
50
500
B
GUT
LD
100

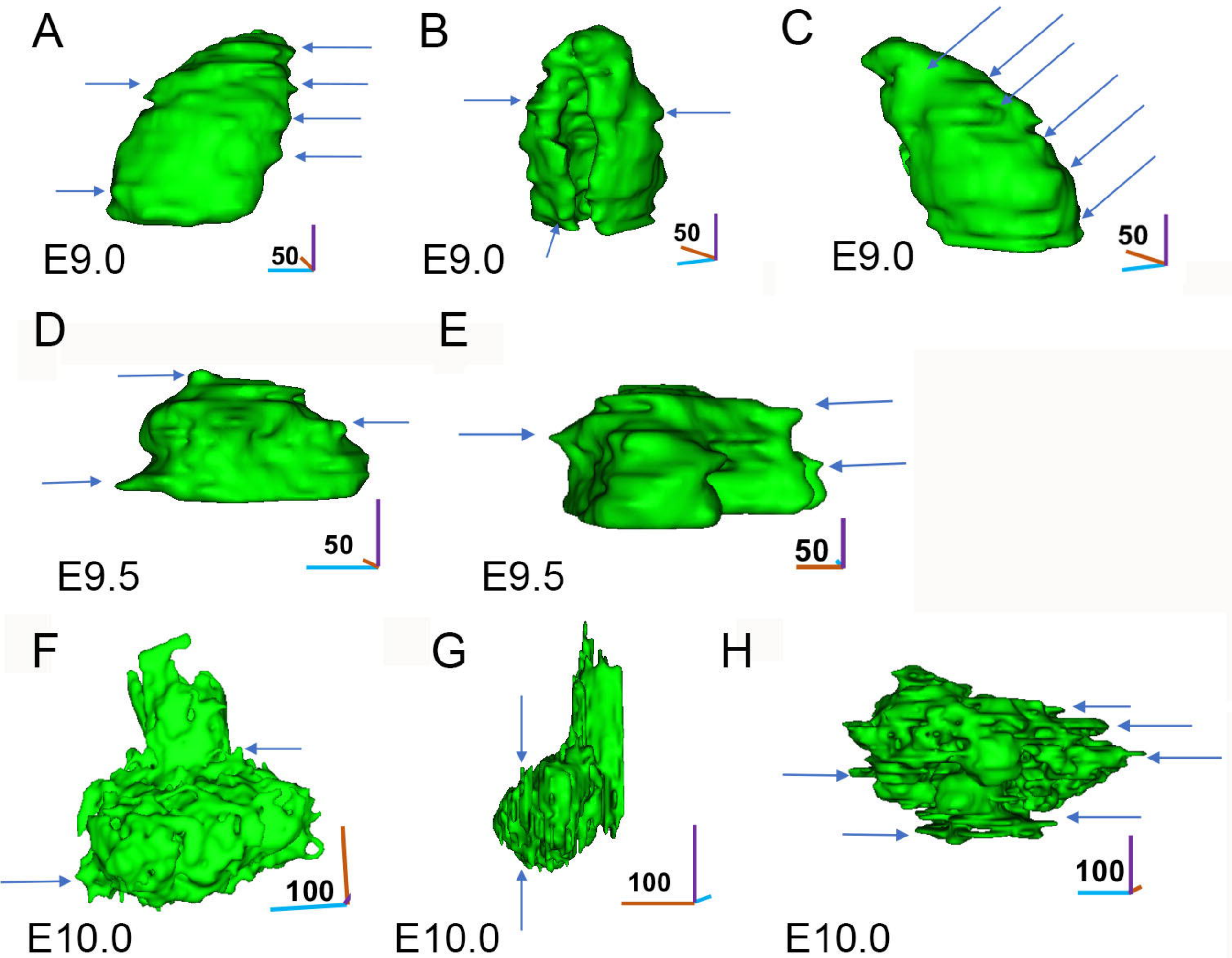
A
E9.0
50
B
E9.0
50
C
E9.0
50
D
E9.5
50
E
E9.5
50
F
E10.0
100
G
E10.0
100
H
E10.0
100

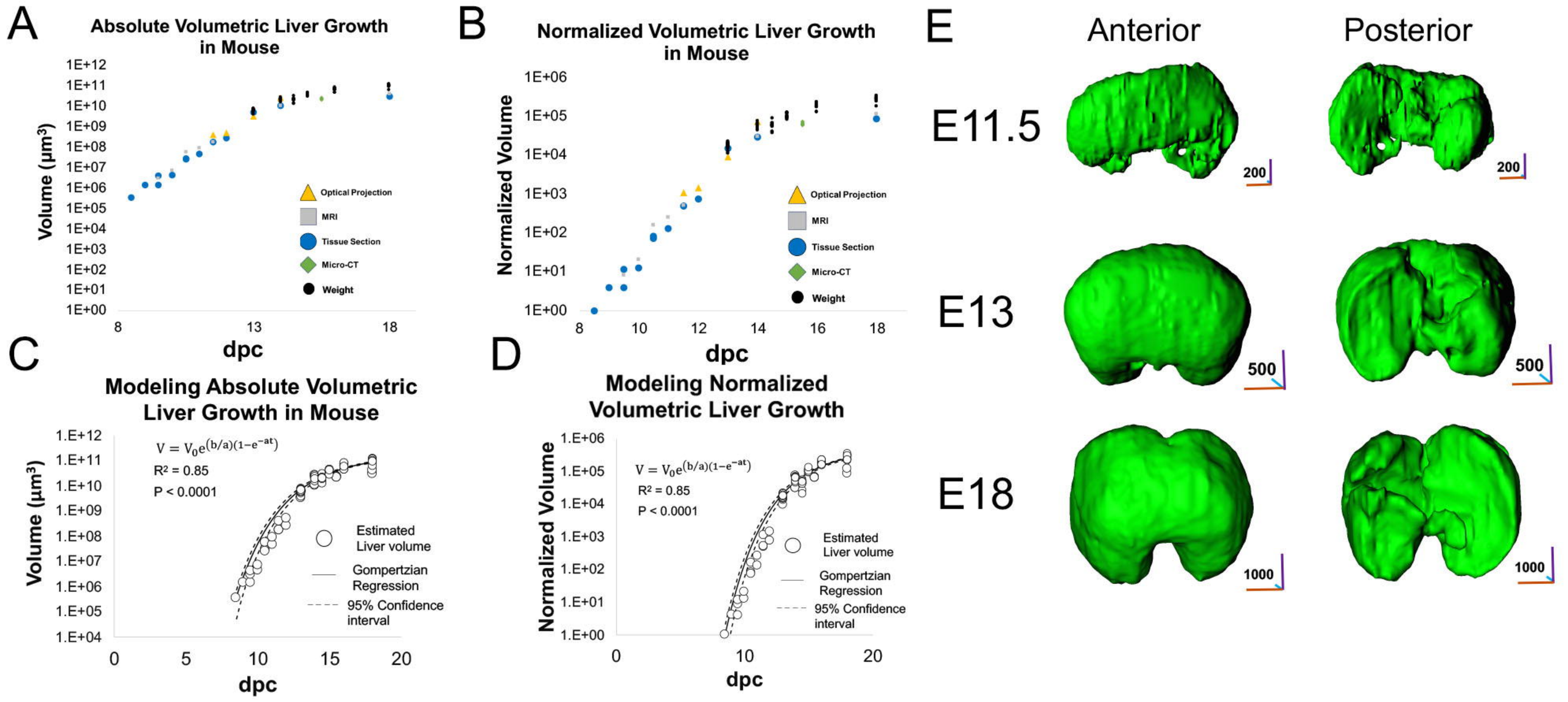
A
Absolute Volumetric Liver Growth in Mouse
Volume (µm³)
1E+12
1E+11
1E+10
1E+09
1E+08
1E+07
1E+06
1E+05
1E+04
1E+03
1E+02
1E+01
1E+00
8
13
18
dpc
Optical Projection
MRI
Tissue Section
Micro-CT
Weight
B
Normalized Volumetric Liver Growth in Mouse
Normalized Volume
1E+06
1E+05
1E+04
1E+03
1E+02
1E+01
1E+00
8
10
12
14
16
18
dpc
Optical Projection
MRI
Tissue Section
Micro-CT
Weight
C
Modeling Absolute Volumetric Liver Growth in Mouse
Volume (µm³)
1.E+12
1.E+11
1.E+10
1.E+09
1.E+08
1.E+07
1.E+06
1.E+05
1.E+04
$V = V_0 e^{(b/a)(1-e^{-at})}$
R² = 0.85
P < 0.0001
Estimated Liver volume
Gompertzian Regression
95% Confidence interval
0
5
10
15
20
dpc
D
Modeling Normalized Volumetric Liver Growth
Normalized Volume
1.E+06
1.E+05
1.E+04
1.E+03
1.E+02
1.E+01
1.E+00
$V = V_0 e^{(b/a)(1-e^{-at})}$
R² = 0.85
P < 0.0001
Estimated Liver volume
Gompertzian Regression
95% Confidence interval
0
10
20
dpc
E
Anterior
Posterior
E11.5
200
200
E13
500
500
E18
1000
1000

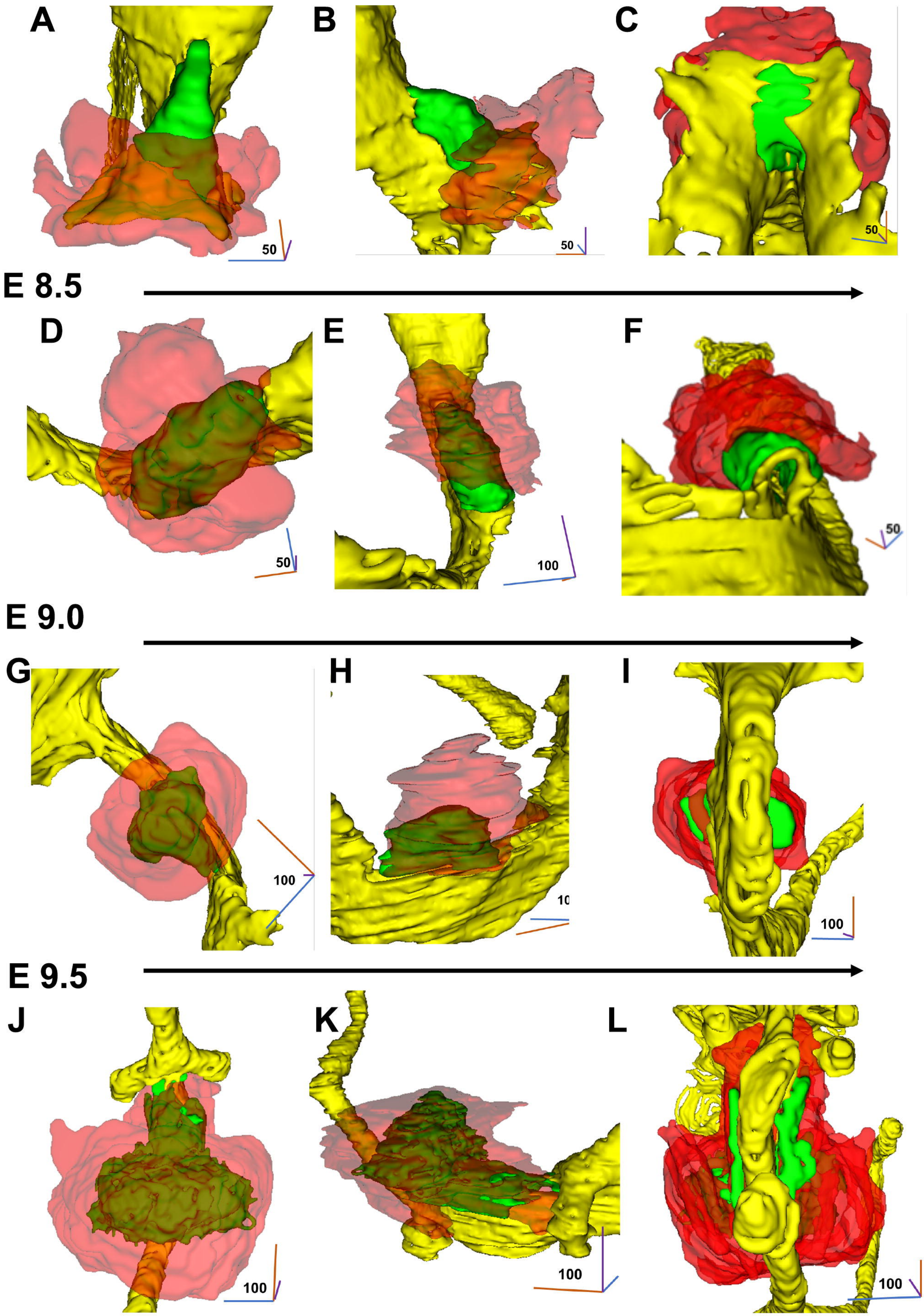
A
B
C
50
50
50
E 8.5
D
E
F
50
100
50
E 9.0
G
H
I
100
10
100
E 9.5
J
K
L
100
100
100
E 10.0

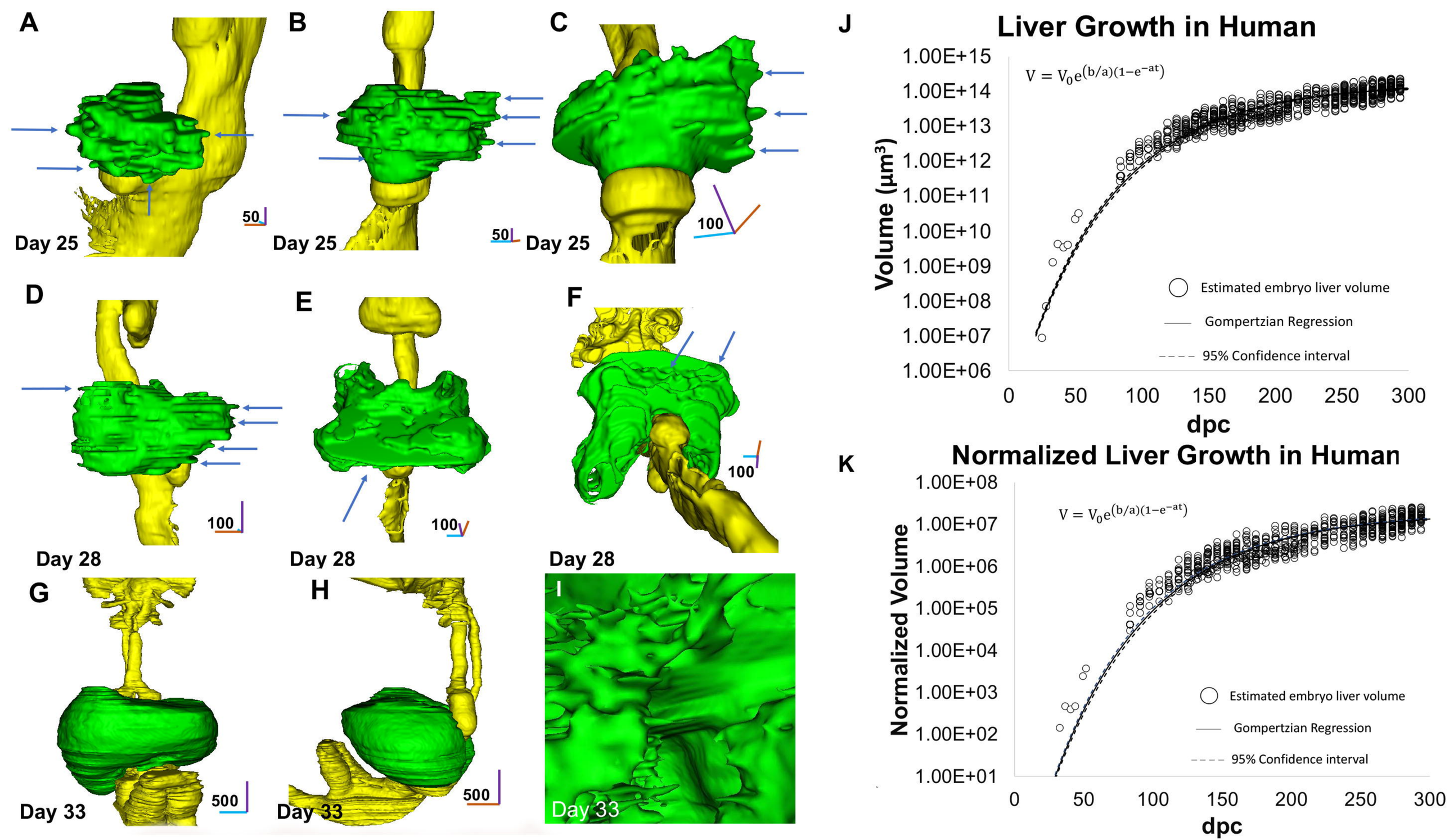
A
B
C
D
E
F
G
H
I
J
K
Day 25
Day 25
Day 25
Day 28
Day 28
Day 28
Day 33
Day 33
Day 33
50
50
100
100
100
100
500
500
Liver Growth in Human
$V = V_0 e^{(b/a)(1-e^{-at})}$
Volume (μm³)
1.00E+15
1.00E+14
1.00E+13
1.00E+12
1.00E+11
1.00E+10
1.00E+09
1.00E+08
1.00E+07
1.00E+06
0
50
100
150
200
250
300
dpc
Estimated embryo liver volume
Gompertzian Regression
95% Confidence interval
Normalized Liver Growth in Human
$V = V_0 e^{(b/a)(1-e^{-at})}$
Normalized Volume
1.00E+08
1.00E+07
1.00E+06
1.00E+05
1.00E+04
1.00E+03
1.00E+02
1.00E+01
0
50
100
150
200
250
300
dpc
Estimated embryo liver volume
Gompertzian Regression
95% Confidence interval

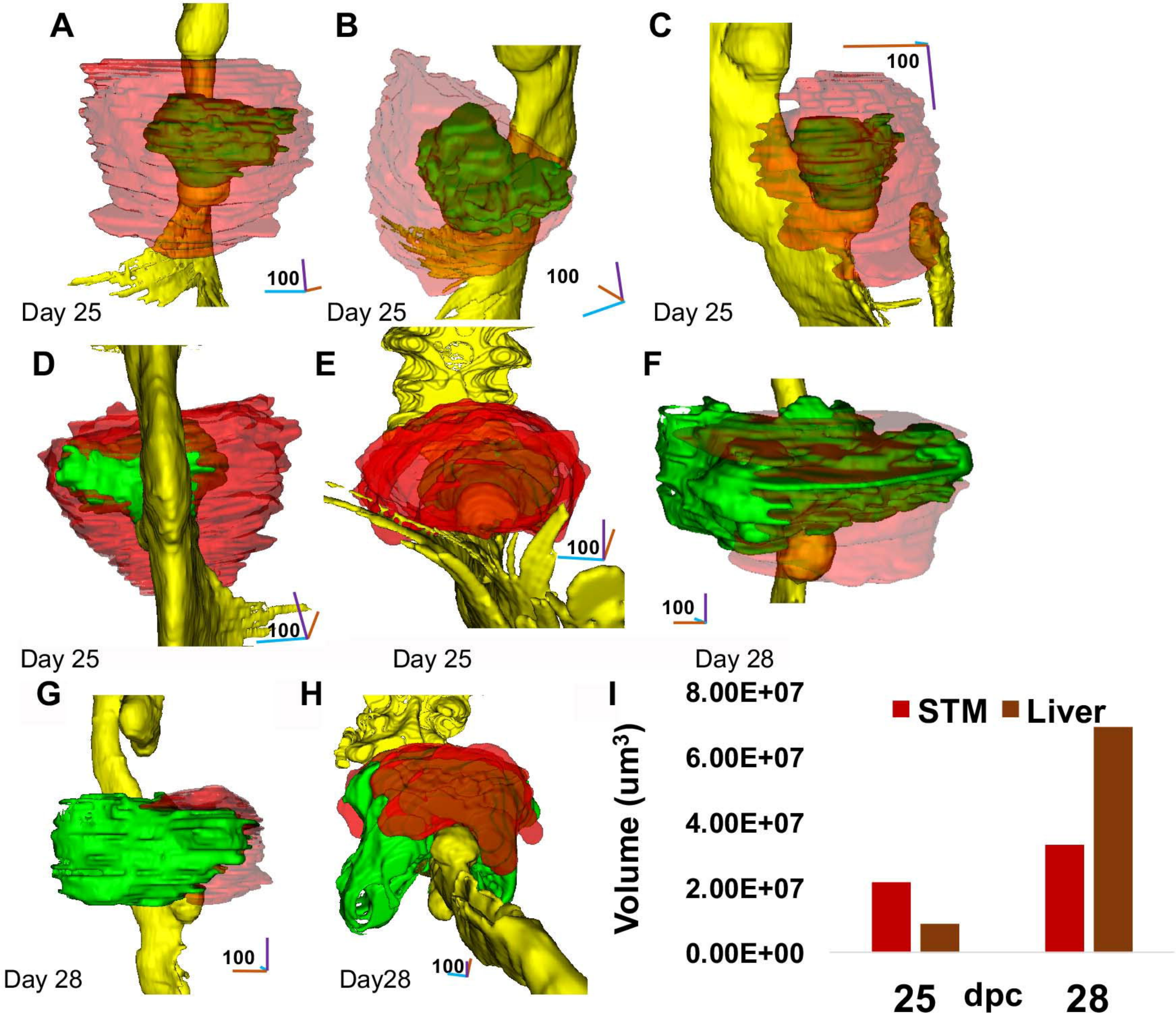
A
B
C
100
Day 25
Day 25
Day 25
D
E
F
Day 25
Day 25
Day 28
G
H
I
Day 28
Day28
Volume (um3)
8.00E+07
6.00E+07
4.00E+07
2.00E+07
0.00E+00
STM
Liver
25
dpc
28